12-2013

An Experimental Study of Hemispherical Vortex Generators for Separation Control over a NACA-0012

David Joseph Ronald Tucker
University of Tennessee - Knoxville, dtucker8@utk.edu

To the Graduate Council:

I am submitting herewith a thesis written by David Joseph Ronald Tucker entitled "An Experimental Study of Hemispherical Vortex Generators for Separation Control over a NACA-0012." I have examined the final electronic copy of this thesis for form and content and recommend that it be accepted in partial fulfillment of the requirements for the degree of Master of Science, with a major in Aerospace Engineering.

Ahmad Vakili, Major Professor

We have read this thesis and recommend its acceptance:

Trevor Moeller, Gregory Power

Accepted for the Council:
Carolyn R. Hodges

Vice Provost and Dean of the Graduate School

(Original signatures are on file with official student records.)

An Experimental Study of Hemispherical Vortex Generators for Separation Control over a NACA-0012

A Thesis Presented for the

Master of Science

Degree

The University of Tennessee, Knoxville

David Joseph Ronald Tucker

December 2013

ACKNOWLEDGEMENTS

Completing this paper and, by extension, my master's degree represents the fulfillment of a goal that has been set long before arriving in Tennessee in August 2011. The help and encouragement of many people in my life got me to this point and I am grateful. I will miss the chats with my advisor Dr Vakili; even and perhaps especially the ones that would drift off topic. His timely assistance was key to my finishing my experimentation with results I could use.

Joel Davenport got me started in the water tunnel and was there for a few key moments that kept me on track. Jonathan Kolwyck suffered through pretty much every other moment in the water tunnel and I appreciated both his intuition and company throughout the good times and bad! A thanks is due to Mr Dimitrios Kavelakis, who taught me just enough about photography to be dangerous.

I also would like to pass on thanks to my committee members; Dr Trevor Moeller and Dr Greg Power. Without their insightful feedback throughout the various revisions of this paper it would have been difficult for an argument to be made. My father Dr John Tucker helped me smooth out many rough edges in terms of readability, but I maintained a few awkward sentences just so I could claim ownership. Bonny O'Keefe, my mother, kept my spirits up when I had doubts and I really appreciated her counsel.

Finally I cannot overstate the contribution of my lovely bride Sara Lynn Dobbin; without whom none of this would have been possible.

ABSTRACT

This is a study towards understanding hemispherical vortex generators (VGs) and their effectiveness on delaying flow separation over an airfoil. To be tested was whether these devices could generate a horseshoe vortex structure that effectively entrained higher momentum flow into the boundary layer over the surface of a NACA-0012 wing section. The experimental results are primarily from water tunnel experiments, but the clean configuration NACA-0012 airfoil was investigated by numerical methods in order to ascertain the potential for numerical modeling as a tool to accurately predict flow around the VGs, and as a guide for size and location optimization. At Reynolds number of 50,000 the separation point was measured using three different sizes (large, medium, and small diameters) of VGs placed on the airfoil in different configurations at a range of angles of attack from 10 to 20 degrees. Fluorescent dye was illuminated by a system of lasers and a rotating mirror in order to visualize the flow over the airfoil. The following results were observed: large VGs were most effective and had the most consistent correlation between separation delay and VG spacing, medium VGs followed the same general trend, but had significantly lower effectiveness throughout the range of VG spacing, and small VGs generally seemed inert in their interaction with the local flow; appearing stagnant except for the smallest spacing where adjacent VGs were in contact. Spacing effectiveness of the large VGs was determined at one angle of attack; the best separation between large VGs was about 3 diameters. Numerical computations were performed by solving the Reynolds Averaged Navier-Stokes (RANS) equations with the Stanford University Unstructured (SU^2) code. The code ran remotely on the Kraken system at Oak Ridge National Laboratory. The simulations and associated experiments were meant to determine whether such devices could effectively delay flow separation. There are many practical applications for these VGs including: micro air vehicle static stall, rotorcraft dynamic stall, and applications to turbomachinery.

TABLE OF CONTENTS

LIST OF TABLES

LIST OF FIGURES

NOMENCLATURE

VG	=	Vortex Generator
DG	=	Disturbance Generator
$u_{i/j}$	=	Velocity Field (feet per second)
$x_{i/j}$	=	Positional Term (inches)
t	=	Time (seconds)
p	=	Pressure Field (pounds-force per square foot)
ρ	=	Density (pounds-mass per foot cubed)
v	=	Kinematic Viscosity (foot squared per second)
λ	=	Second Coefficient of Viscosity (pounds-force seconds per square foot)
μ	=	Dynamic Coefficient of Viscosity (pounds-force seconds per square foot)
τ_{ij}	=	Stress Term (pounds-force per square foot)
δ_{ij}	=	Kronecker Delta Function
Re_{ind}	=	Indifference Reynolds Number
Re_{crit}	=	Critical Reynolds Number
D	=	Diameter of Vortex Generator (inches)
x	=	Chord-wise axis on airfoil (inches)
y	=	Span-wise axis on airfoil (inches)
z	=	Normal axis to airfoil (inches)
V	=	Speed or Velocity Vector (with indication) (feet per second)
ω	=	Vorticity (per seconds)
x/c	=	Non-dimensional relation for position with respect to chord
y/D	=	Non-dimensional relation for spacing with respect to diameter

CHAPTER I
INTRODUCTION

Background

Many investigators have conducted research in recent decades to understand the impact of various shapes and configurations of disturbance generators (DGs) and vortex generators (VGs) for both passive and active flow control. Deformable and/or deployable VGs are their own field of research, as is the study of dynamic stall in rotary applications. Numerical and experimental studies abound within these various fields of flow control, with applications ranging from dynamic stall in rotorcraft to the cooling of rotor and stator blades within turbomachinery. The essential idea of these investigations is to place VGs at particular span wise intervals along a section, so that their interaction with the external flow will create longitudinal vortices downstream. In similar studies [1] these vortices have demonstrated the characteristic of mixing the relatively higher momentum flow above the boundary layer with the lower momentum flow closer to the surface. This mixing has the effect of making the flow more resilient to adverse pressure gradients and delays flow separation and the resulting loss of lift and increase in drag.

Statement of Objective

This investigation studies passive vortex creation and intends to demonstrate that a shape that reduces form drag relative to other VG styles can control the flow in an effective and predictable manner. The chosen form will be small hemispheres of radius and spacing to be parametrically studied. The angle of attack and flow Reynolds number with respect to chord will be kept constant so that any effectiveness of the hemispheres on turbulent transition can be measured. Effectiveness will be measured through the use of fluorescent dye and laser imagery in addition to naked eye observation.

In the following chapter the background theory will be discussed, along with a review of the existing and pertinent literature on the subject of vortex generation. Chapter 3 will discuss the experimental approach; touching on some of the simulations that preceded water tunnel trials and a description of the flow visualization scheme. In Chapter 4 the gathered results will be presented and analyzed, followed by conclusions and recommendations in Chapter 5.

CHAPTER II
TECHNICAL REVIEW

Theory

The Reynolds Number

Osborne Reynolds proposed the Reynolds number in 1883, and it has been used since as a significant non-dimensional characteristic of viscous flows. Dimensional analysis allows us to apply the experimental/simulated results in one instance to forecast the results for all dynamically similar flow scenarios; making it the primary controlling parameter for viscous analysis [2]. Reynolds number is defined as the ratio of inertial forces to viscous forces in a flow:

$$\mathrm{Re}_L = \frac{\rho UL}{\mu} = \frac{UL}{\nu} \qquad (1)$$

As Reynolds number decreases, viscous forces play an increasingly larger role in defining the flow.

Figure 1 [3] shows general ranges of chord Reynolds numbers associated with particular speeds. Due to considerations that will be described in Chapter 3, the test object in the water tunnel will be experiencing chord Reynolds numbers of approximately 10^4. At a speed of 1 foot per second this places the experimental data firmly in the range of model airplanes and larger micro air vehicles. The non-dimensional nature of the Reynolds number allows us to make general statements about the applicability of the results in this flow regime to other similar flows. At this Reynolds number, flow is laminar and the lift to drag ratio is fairly steady, whereas at the next order of magnitude Re, flow becomes transitional and it becomes more difficult to identify the range of lift coefficient to drag coefficient, as illustrated in Figure 2 [3].

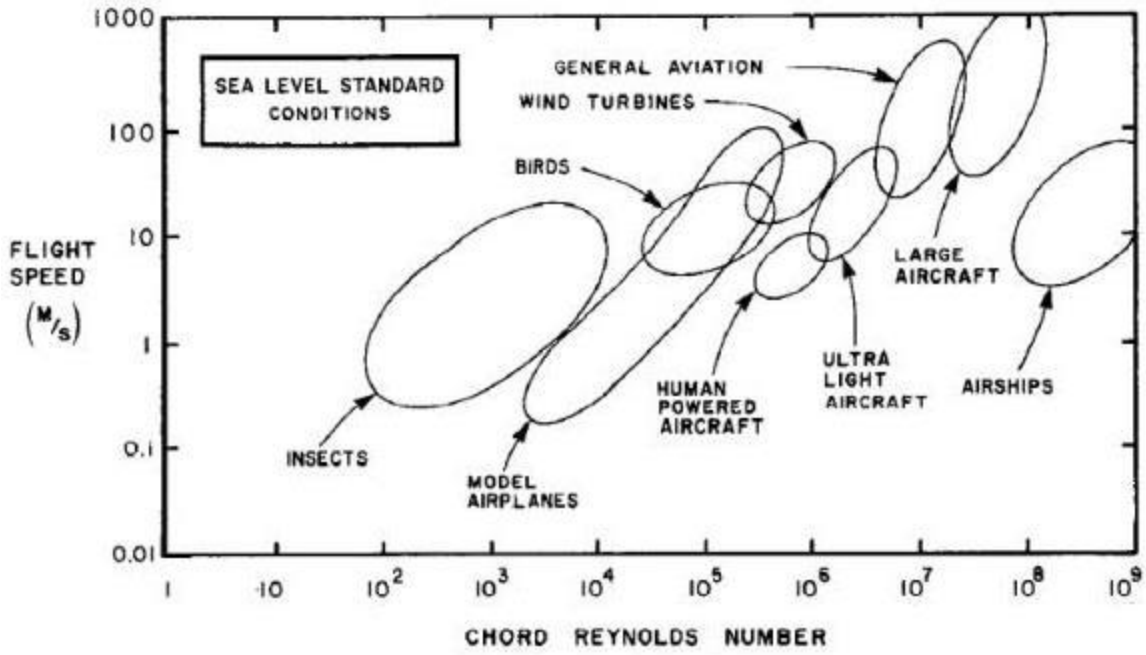

Figure 1. Various Chord Reynolds numbers for air vehicles [3].

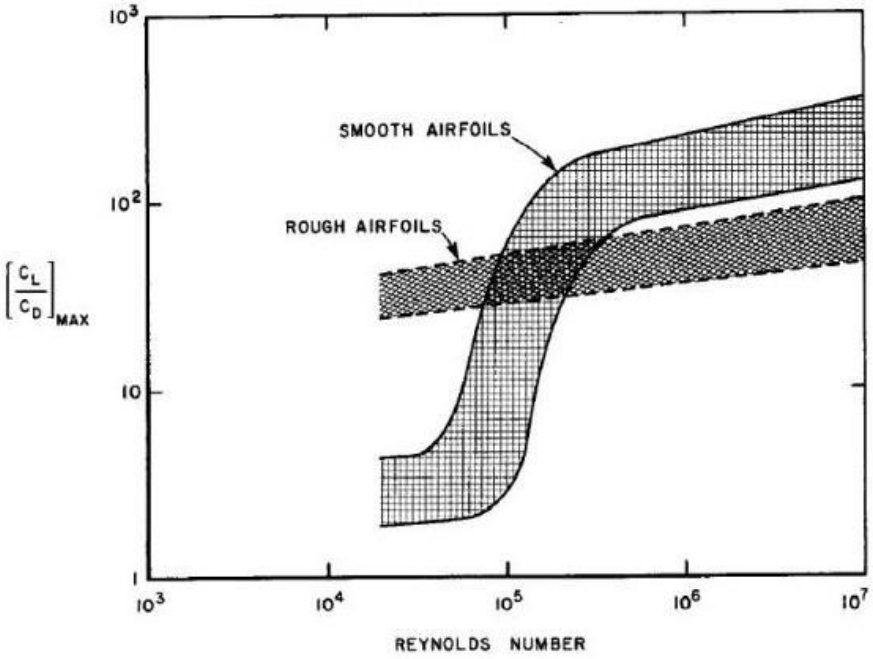

Figure 2. Reynolds number vs Lift to Drag ratio [3].

Boundary Layer Growth

Basic fluid dynamics can be divided into two general categories; inviscid and viscous. Utilizing inviscid theory one can determine the lift an airfoil can create but not the drag; we use inviscid theory in external flow far from the surface of the airfoil. In order to predict the drag on a body moving through a fluid, we need to apply viscous theory and more specifically; boundary layer theory. As Prandtl developed in his landmark presentation of 1904, the relatively thin layer of fluid against a wall is the source of all drag for fluid-body interaction [4]. By convention we define the boundary layer as starting from the surface and extending to 99% of the free stream velocity [2]. This velocity gradient is perpendicular to the surface in question, and the fluid is stagnant at the wall itself; known as the no-slip condition. Due to the increasing velocity further from the surface, the fluid layers shear against one another until the fluid has reached the local free stream fluid velocity. Figure 3 illustrates a typical velocity profile against a flat plate [5] while Figure 4 shows, conceptually and with stretched coordinates in cross flow directions, the outer edge of the boundary layer generated over a sample airfoil [6].

A Reynolds number of approximately 10^4 is sufficiently large for standard thin-boundary-layer analysis to be applicable [2]. Even for the relatively smaller VG the Reynolds number should be large enough to imply that the vorticity gets pushed downstream of the surface leaving the flow far from the walls irrotational. In this instance, the rate of downstream convection is much greater than the rate of transverse viscous diffusion:

$$\sqrt{\frac{\nu L}{U^3}} << \frac{L}{U} \qquad (2)$$

That is to say the boundary layer can be assumed to be thin if the diffusion time is much shorter than the residence time. As equation (3) shows below, this can

be verified from the Reynolds number. For the airfoil itself the thin boundary layer approximation is reasonable, but when considering the chord Reynolds number of the VG alone (10^2) this assumption may not hold true.

$$\sqrt{\frac{UL}{\nu}} = \sqrt{\mathrm{Re}_L} >> 1 \tag{3}$$

As the Reynolds number decreases, the viscous forces will play a greater role in determining the dynamics of the fluid.

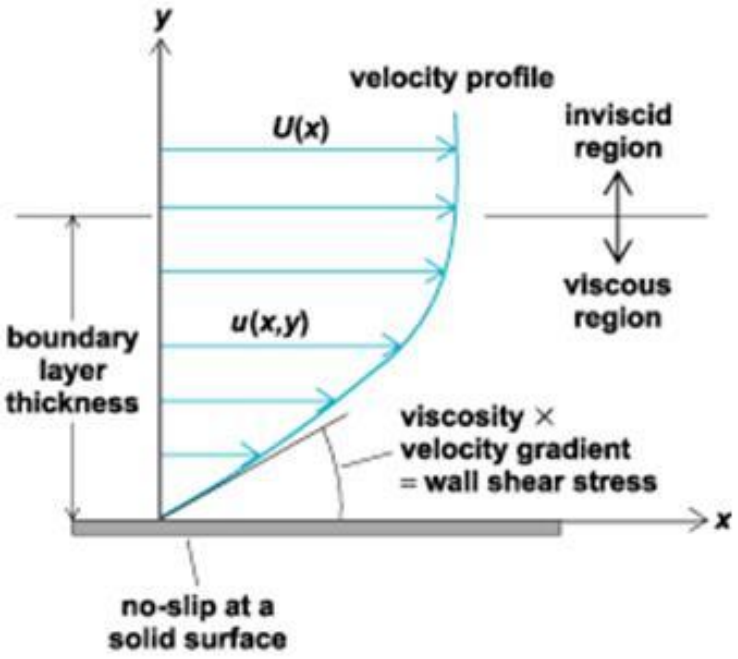

Figure 3. Example of laminar boundary layer velocity profile [5].

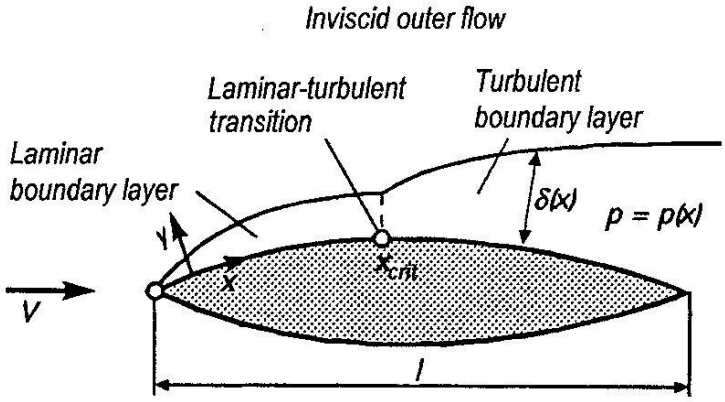

Figure 4. Example boundary layer over an airfoil [6].

As the local Reynolds number increases along the surface of the airfoil, the flow approaches a critical Reynolds number where transition to turbulence begins; Re_{cr} approximately order of 10^6 [2]. For a surface with curvature the flow also must travel over areas of either favorable or adverse pressure gradients and separation can occur. Thin boundary layer assumptions do not hold in these regions. Figure 5 [2] demonstrates how the velocity profile can look under these conditions.

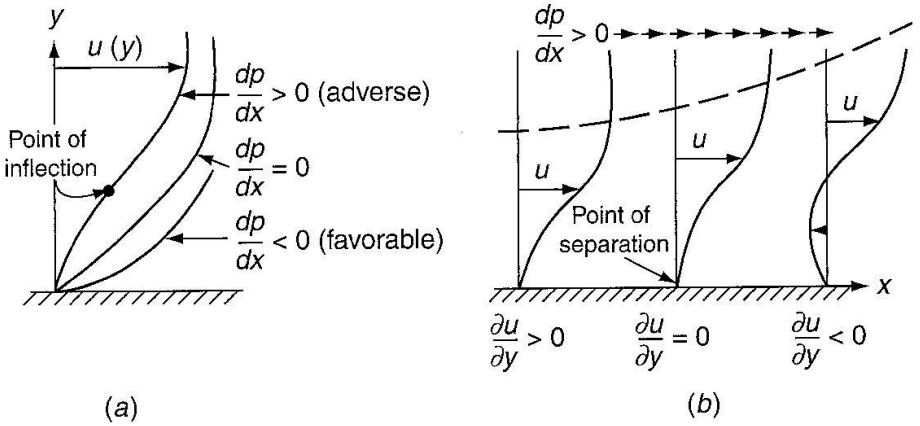

Figure 5. Effects of curvature on pressure gradient [2].

A negative pressure gradient is favorable since no separation can occur; this is where the pressure decreases in the direction of flow, and it increases the

stability of a laminar flow. At the leading edge of an airfoil a negative pressure gradient will be present due to the increasing velocity of the fluid as it accelerates over the surface; increasing the dynamic pressure and decreasing the static pressure. As the curvature of the surface changes sign the velocity profile can develop an S-shape, where there is first separation and then potential reverse flow towards the surface. This is the condition of an adverse pressure gradient and is destabilizing to laminar flow. The separation point occurs where the fluid is at first stationary and then reverses direction with respect to the free stream velocity. At lower Reynolds numbers the fluid flow does not necessarily have the inertial force to overcome this condition, and laminar separation can occur before transition to a turbulent boundary layer.

Boundary Layer Separation and Transition

As previously stated it is possible for the boundary layer to separate prior to or after transition to turbulence. It is also possible for the boundary layer to reattach downstream as a turbulent layer [7]. The airfoil characteristics and flow dynamics will dictate how the boundary layer behaves, but it is important to note that these behaviors may be transient or periodic. This mechanism of separation accounts for much of the instability that low Reynolds number airfoils experience. In this investigation the Reynolds number (10^4) is so low that reattachment is unlikely [8]. At Reynolds numbers approaching $5x10^4$ reattachment becomes a potential factor and would be illustrated by Figure 6 [7] below.

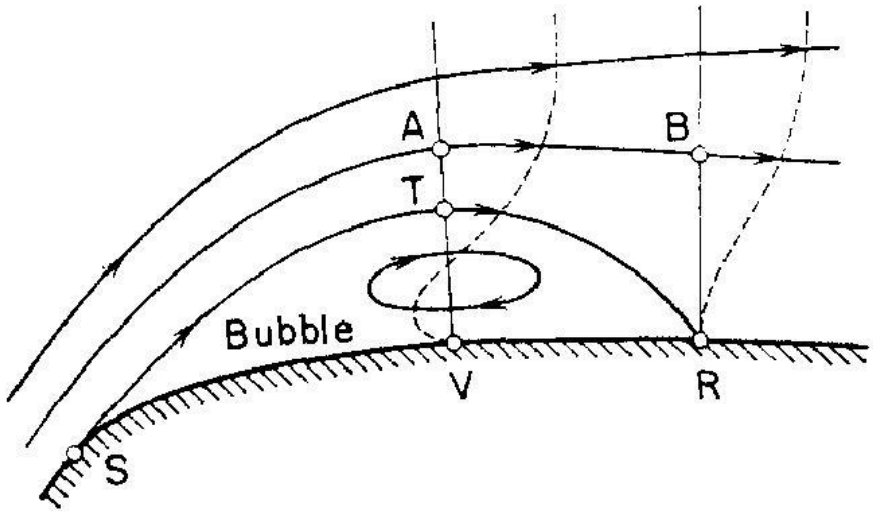

Figure 6. Schematic illustration of a leading edge separation bubble [7].

In this case the incoming flow separates beginning at point S and subsequently reattaches to the surface at R. The recirculating region between S and R is known as the separation bubble and can be considered a pressure plateau [5]. The flow can be laminar or turbulent prior to separation, but if it becomes turbulent upon separating it is more likely to contain the required inherent energy to withstand the adverse pressure gradient and reattach [7]. The turbulent flow has a greater momentum and in exchanging this momentum with the external flow, separation is delayed [9][10].

Tollmien and Schlichting proposed a process to explain the transition to turbulence which is a solution to the Orr-Sommerfeld equations for stability. These Tollmien-Schlichting waves are illustrated in Figure 7 [6].

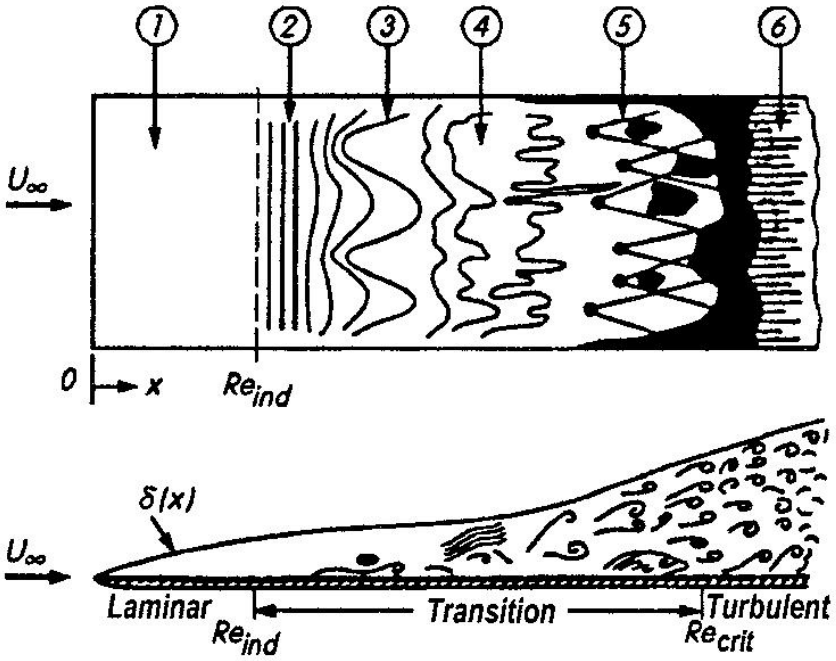

Figure 7. Tollmien-Schlichting waves over a flat plate from top and side view [as labeled in Fig 15.5 of citation]: (1) stable laminar flow, (2) unstable Tollmien-Schlichting waves, (3) three-dimensional waves and vortex formation (Λ-structures), (4) vortex decay, (5) formation of turbulent spots, and (6) fully turbulent flow [6].

The proposed waves of instability are superimposed on the laminar flow after the indifference Reynolds number (Re_{ind}) which leads to the development of fully turbulent flow by the critical Reynolds number (Re_{crit}). It should be noted that this turbulence is fully three dimensional.

Vorticity Dynamics

Vorticity is the measure of rotationality present in a fluid and is twice the value of angular velocity [2]. The no-slip condition at the surface of an object in real flow imparts vorticity to the fluid by diffusing it throughout the boundary layer [11]. From a two dimensional or infinite airfoil view this vorticity is only a y-z phenomenon about the y axis but in reality small perturbations mean that any

object quickly develops very complex flow around it. The viscosity of the fluid will dictate how effectively vorticity is transmitted; this is the principle by which vortex generation operates. Key to this investigation is the viscous entrainment of higher momentum flow outside the boundary layer into the lower momentum flow within boundary layer and whether this energy transfer is successful in delaying flow separation. The adverse pressure that leads to separation does not change, but the flow develops resilience to it by maintaining its momentum longer than it otherwise would.

Flow Around Hemispheres

Blunt bodies display a particular type of vortex system which is being utilized in this experiment. The horseshoe vortex system is a series of individual vortical structures that are formed when fluid moves past a bluff body. Pressure gradients that are a direct result of the curvature of the body will determine the paths the fluid takes around the object.

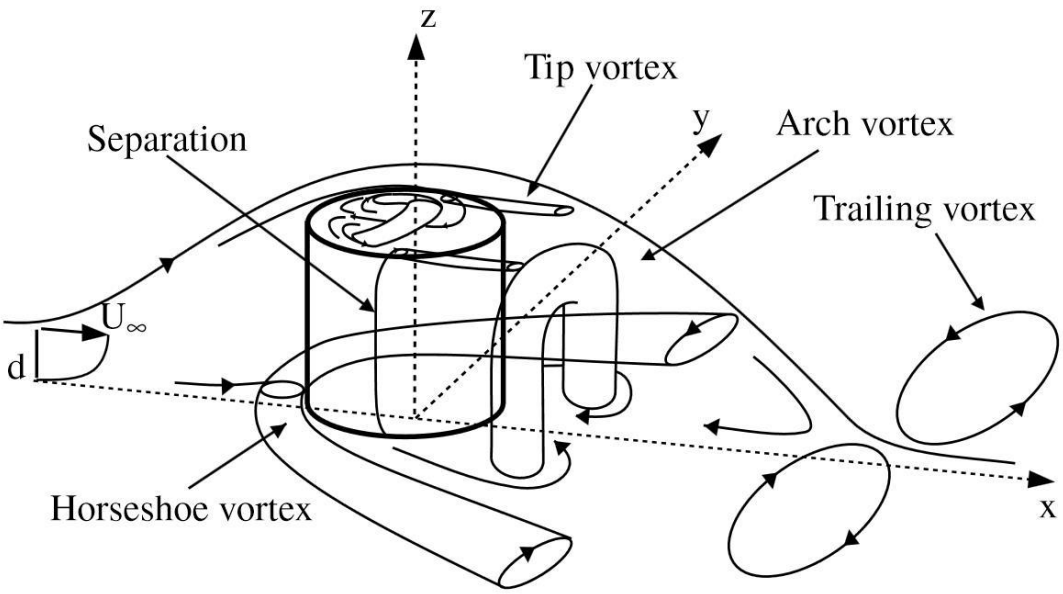

Figure 8. Schematic illustration of a horseshoe vortex system due to flow over a cylinder at a surface [12].

As illustrated in Figure 8 the fluid being displaced around the cylinder reacts to create several different vortex cores. Of particular interest in this paper is the horseshoe vortex generated by the fluid which was displaced towards the base of the cylinder on the upstream edge. This system ends up generating trailing vortices behind the body that will ultimately affect the level of energy in the boundary layer and consequent flow separation.

Figure 9 below demonstrates how this same initial flow field would react to a hemisphere. It is not critical that the base of the hemisphere is sitting on a flat plate; similar flow over the hemisphere and trailing vortices could be developed if there were a shear layer deflecting the flow at the leading edge instead. The trailing vortices in this figure are the streamwise co-rotating pairs that can be taken advantage of in sustaining flow attachment. Figure 10 shows a striking image of how these separate vortex cores develop and travel downstream.

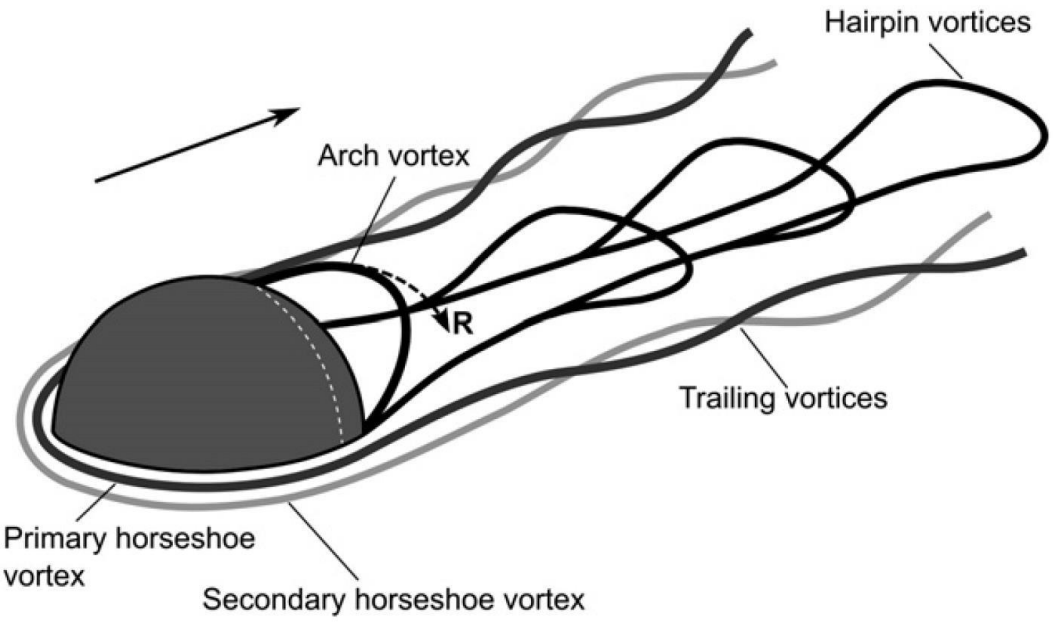

Figure 9. Schematic illustration of a horseshoe vortex system in vicinity of a hemisphere at a surface [13].

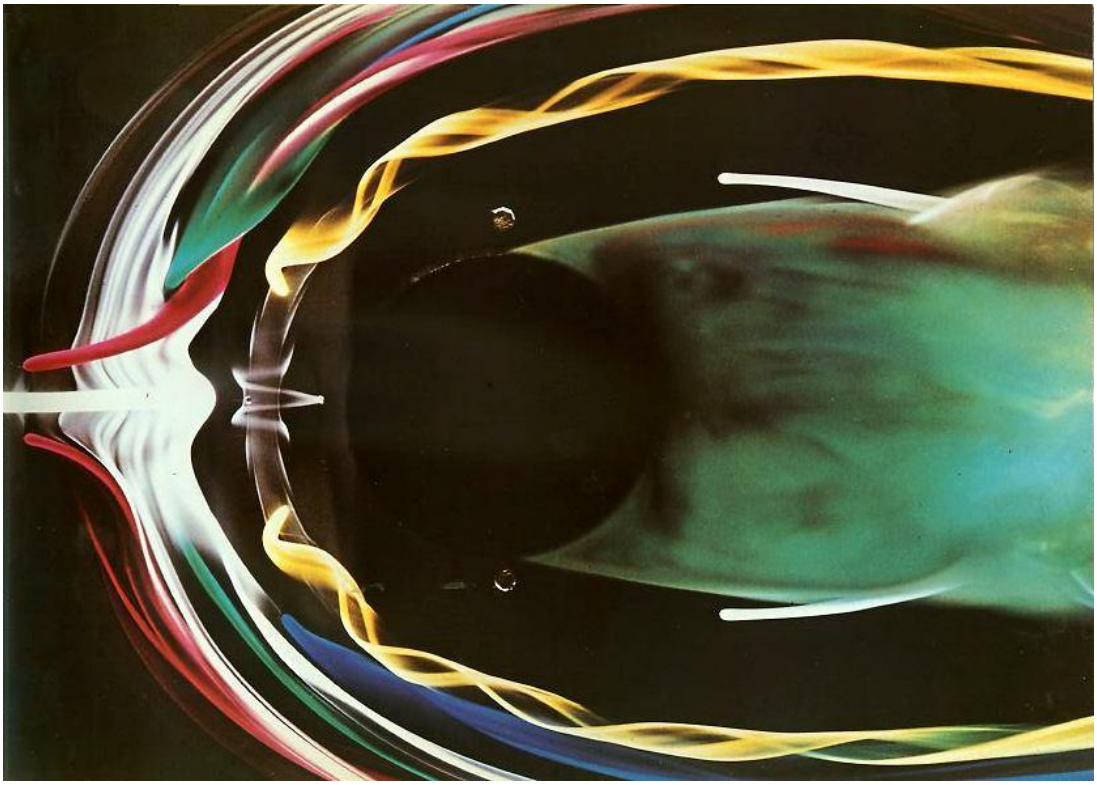

Figure 10. Horseshoe vortex structure in vicinity of a cylindrical obstacle at a surface [14].

Static and Dynamic Effects

Despite the fact that this experiment was carried out with each airfoil configuration in a static condition, one of the main applications of this technology is to dynamic stall reduction. The studies by DLR [15] to create effective streamwise vortices over pitching helicopter rotor blades were a major inspiration for carrying out this investigation. Dynamic stall differs from static stall in that there is the inertial surging of the fluid to consider. Figure 11 illustrates the overall effect of the pitching motion; the portion of the hysteresis loop at the top showing the airfoil pitching up, with the lower loop showing the effect on lift coefficient as the airfoil pitches down.

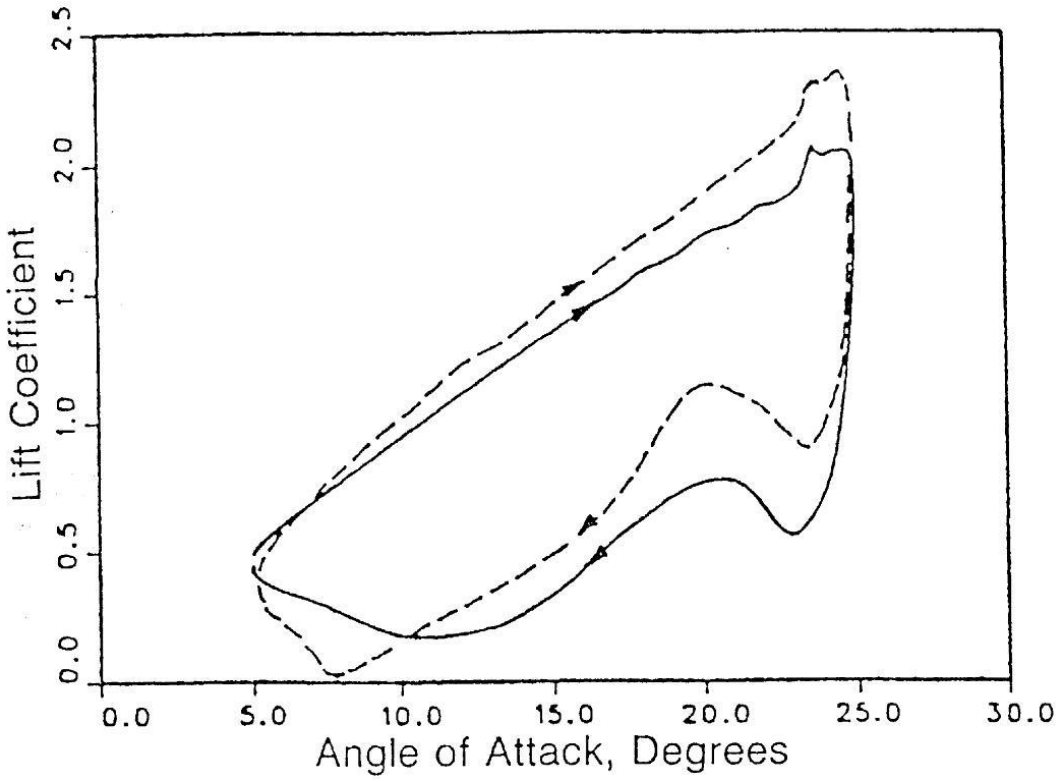

Figure 11. NACA-0012 undergoing oscillatory pitching motion; numerical results shown with solid line, experimental results shown in dashed line; Re = $3x10^6$ [16].

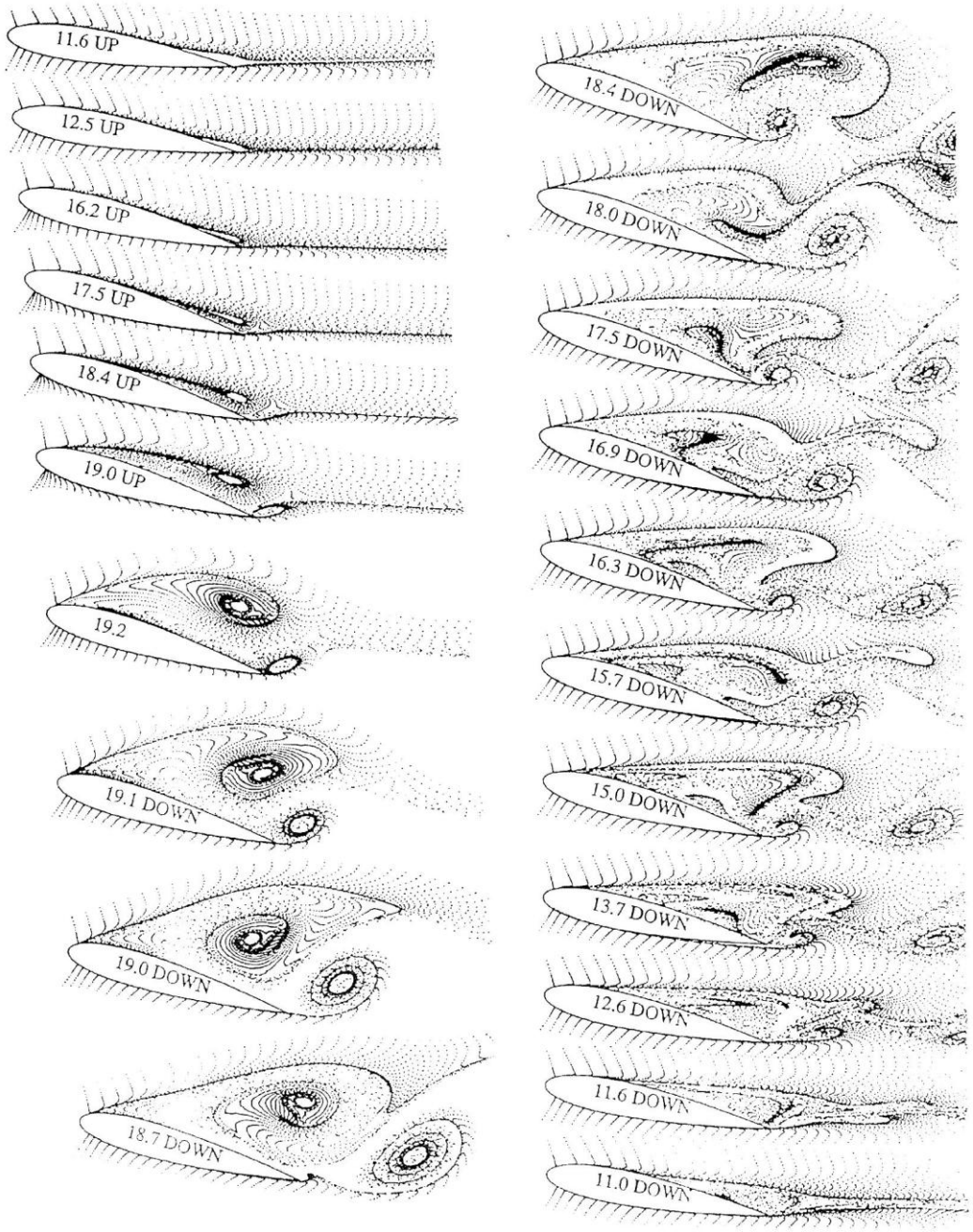

Figure 12. NACA-0015 undergoing oscillatory pitching motion shown with particle traces; illustration of difference between plunging and surging motions; Re = $2x10^6$ [17].

Figure 12 shows a capture of particle traces over a range of angles of attack. Where the airfoil pitches up the stall vortex is held against the surface but

when the airfoil pitches down the stall vortex is shed; leading to separation, potential stall and potentially abrupt pitching moments. It appears that any delay to separation in a static case will also delay a dynamic one.

Literature Review

Since Taylor's seminal work on separation control via VGs [9], there have been an abundance of analytical, experimental, and numerical investigations into the most diminutive regions of various flow fields. Of particular interest to this investigation is whether hemispherical VGs can be designed and reasonably be expected to generate vortices that will have the overall effect of delaying the onset of static stall. The German Aerospace Center (DLR) has been aggressively pursuing similar studies [15] and has patented [18] the design of cylindrical Leading Edge Vortex Generators (LEVoGs) for use in rotorcraft application in combating dynamic stall.

DLR has also conducted cooperative research with The French Aerospace Lab (ONERA) to study the vortices generated by deployable VGs in the static stall case [19]. These studies have largely concentrated on the phenomenon of dynamic stall and focused on helicopter applications. Dynamic stall is a considerable limiting factor for overall helicopter cruise speed; it is also known as retreating blade stall and can be encountered on the rotor blade when it travels opposite to the direction of flight for the vehicle. The airspeed over the retreating blade is less than that of the advancing blade by a factor of the speed of the aircraft, and relative angle of attack is adversely affected as well, leading to stall and adverse pitching moments.

The idea of using protuberances on the leading edge of an airfoil to control flow separation is at least partially inspired by the observation of nature. Humpback whales use the tubercles on their pectoral fins to maneuver efficiently [20], and a wide range of parametric studies have been published discussing the

relative efficacy of various shapes, sizes, and configurations of VGs. Some have argued that the VG must be higher than the anticipated boundary layer thickness [19] while others have shown that stream wise vortices can be induced utilizing VGs that are small enough to be considered within the boundary layer [21]. For this study it will be assumed that the VGs are higher than the boundary layer thickness since they are located towards the stagnation point at the leading edge of the airfoil.

The creation and maintenance of a horseshoe vortex system has been demonstrated to create trailing counter-rotating vortices [13]. This same counter-rotating vortex structure downstream of many different VGs is responsible for re-energizing boundary layers and effectively delaying flow separation. Demonstration of this structure in a flow goes a long way towards proving effectiveness.

Governing Equations

Equations of Continuity and Momentum

The pertinent equations of motion governing the flow within the boundary layer were first derived by Ludwig Prandtl in 1904 [4]. Prandtl, along with his student Heinrich Blasius, developed and furthered the understanding of boundary layers and bridged the gap between theory and experimental work. Assuming incompressible flow and negligible buoyancy/gravitational effects the Continuity (4) and Navier-Stokes (5) equations can be written as follows:

$$\frac{\partial u_i}{\partial x_i} = 0 \tag{4}$$

$$\frac{\partial u_i}{\partial t} + u_j \frac{\partial u_i}{\partial x_j} = -\frac{1}{\rho}\frac{\partial p}{\partial x_i} + \nu \frac{\partial^2 u_i}{\partial x_j^2} \tag{5}$$

Where u_i and p are instantaneous and ρ and v are constant. This formulation of equation (5) also follows Stokes' simplifying hypothesis that:

$$\lambda + \tfrac{2}{3}\mu = 0 \tag{6}$$

In other words the coefficient of bulk viscosity is zero and the more difficult terms drop out of the full expression of conservation of momentum. While this assumption can be argued as an oversimplification, it is generally treated as warranted [22]. This assumption also leads us to the conclusion that mechanical pressure is equal to thermodynamic pressure [2].

SU²

In order to capture the potential for more complex flow physics, some of the underlying assumptions of equations (4) and (5) need to be removed. Although these are common formulations for analytical evaluation, numerical schemes can handle a more robust form of theses equations. As laid out in most Computational Fluid Dynamics (CFD) textbooks, the following forms are for the Reynolds form of the Continuity equation and the Reynolds-Averaged Navier-Stokes (RANS) equations [23]:

$$\frac{\partial \bar{\rho}}{\partial t} + \frac{\partial}{\partial x_j}\left(\bar{\rho}\tilde{u}_j\right) = 0 \tag{7}$$

$$\frac{\partial}{\partial t}\left(\bar{\rho}\tilde{u}_i\right) + \frac{\partial}{\partial x_j}\left(\bar{\rho}\tilde{u}_i\tilde{u}_j\right) = -\frac{\partial \bar{p}}{\partial x_i} + \frac{\partial}{\partial x_j}\left(\bar{\tau}_{ij} - \overline{\rho u_i'' u_j''}\right) \tag{8}$$

The process of applying Reynolds averaging divides each variable into a mean and fluctuating component equation (9), then collects the terms and takes a time average of the new expression of the equations; denoted by the bar above the quantity. Consequently, this form leads to application in steady-state

simulations only. It is also important to note that tilde denotes mass-weighted averages, as shown in equation (10):

$$f = \bar{f} + f' \tag{9}$$

$$\tilde{f} = \frac{\overline{\rho f}}{\bar{\rho}} \tag{10}$$

Stanford University Unstructured (SU^2) utilizes the Spalart-Allmaras (S-A) model to resolve the turbulent viscosity term that develops at the end of equation (8) [24]. Neglecting the energy portion of the matrices used for the SU^2 Partial Differential Equation (PDE) solver, the Continuity and RANS equations are represented by the following equations [24]:

$$\frac{\partial U}{\partial t} + \nabla \cdot \vec{F}^c - \nabla \cdot \vec{F}^v = Q \tag{11}$$

$$U = \begin{bmatrix} \rho \\ \rho u \\ \rho v \\ \rho w \end{bmatrix}, \vec{F}_i^c = \begin{bmatrix} \rho u_i \\ \rho u_i u + p\delta_{i1} \\ \rho u_i v + p\delta_{i2} \\ \rho u_i w + p\delta_{i3} \end{bmatrix}, \vec{F}_i^v = \begin{bmatrix} . \\ \tau_{i1} \\ \tau_{i2} \\ \tau_{i3} \end{bmatrix} \tag{12}$$

Where:

$$\tau_{ij} = \mu_{tot}\left(\frac{\partial u_i}{\partial x_j} + \frac{\partial u_j}{\partial x_i} - \frac{2}{3}\delta_{ij}\nabla \cdot \vec{V}\right) \tag{13}$$

The boundary conditions used in these simulations are: Euler, symmetry wall, no-slip wall (isothermal), far-field, and characteristic-based outlet boundaries (back pressure).

Analytical Development

The development for the equations describing vorticity are as follows, taken mainly from Viscous Fluid Flow by Frank White [2]. First, we'll use the vector formation of previously shown equation (5), which also uses the total derivative form instead of breaking up the local and convective accelerations:

$$\rho \frac{D\vec{V}}{Dt} = -\vec{\nabla} p - \rho g \hat{k} + \mu \vec{\nabla}^2 \vec{V} \tag{14}$$

Vorticity is then introduced by way of the following two vector identities, recalling that the divergence of velocity is equal to zero where density is constant:

$$\begin{aligned} \left(\vec{V} \cdot \vec{\nabla}\right)\vec{V} &= \vec{\nabla} \frac{V^2}{2} - \vec{V} \times \vec{\omega} \\ \vec{\nabla}^2 \vec{V} &= \vec{\nabla}\left(\mathrm{div}\vec{V}\right) - \mathrm{curl}\vec{\omega} \end{aligned} \tag{15}$$

With substituting the identities of equation (15) equation (14) becomes:

$$\rho \frac{\partial \vec{V}}{\partial t} + \vec{\nabla}\left(p + \tfrac{1}{2}\rho V^2 + \rho g z\right) = \rho \vec{V} \times \vec{\omega} - \mu \mathrm{curl}\vec{\omega} \tag{16}$$

This form is illuminating since the vorticity terms have been separated out to the right hand side of the equation. On the left hand side are the classic Euler terms with respect to inviscid flow; and when the flow is irrotational they will equate to zero once the right hand side terms drop out. The expression then becomes the

familiar form of the unsteady Bernoulli equation, when considering the velocity vector as a potential function and constant density:

$$\rho \frac{\partial \Phi}{\partial t} + p + \tfrac{1}{2}\rho V^2 + \rho g z = \text{constant} \tag{17}$$

Our flow is anything but irrotational, however, since at this low Reynolds number viscosity is a dominant feature; we are using this fact in order to generate vorticity in the flow. Taking the curl of equation (16) we end up with an expression for the rate of change of vorticity:

$$\frac{D\vec{\omega}}{Dt} = \left(\vec{\omega}\cdot\vec{\nabla}\right)\vec{V} + \nu\vec{\nabla}^2\vec{\omega} \tag{18}$$

Equation (18) is known as the Helmholtz hydrodynamics equation; the first term on the right hand side is called the vortex-stretching term and the second is an expression of viscous-diffusion. All of these terms will play a role in any analytical study of the generation of vortices.

CHAPTER III
EXPERIMENTAL APPROACH

Introduction

The primary goal of this study was to collect water tunnel imagery of different configurations of VGs and evaluate their effect on flow separation. In conjunction with the Computational Fluid Dynamics courses, AE599 I and II, a study of the clean airfoil was conducted numerically in order to gain some perspective on the flow physics at the appropriate Reynolds number. As such there has been some duplication of the deliverables from those two courses [25]. A study of a flat plate with a hemispherical VG was also conducted. One goal of this work is to eventually be able to validate the solver code used with the experimental data collected so that many more configurations can be simulated and an optimization study could be completed.

Determining a systematic approach to deliver usable imagery in the water tunnel was challenging. Primary data is in the form of images taken in line with the span of the airfoil so that the laser sheet did not reflect into the camera lens. The drawback of this configuration was that there was an eclipse effect for portions of the upper surface of the airfoil, but quantitative measurements were possible via the imagery collected. Simple observation was used in low light situations where the cameras were unable to capture the delicate and transient nature of the flow physics.

Computational Simulations

Solution Characterization

As previously mentioned, the CFD solver used in these simulations is the SU^2 code. Being both newly released as well as open-source, it was an ideal candidate for utilization. Although there have been growing pains with each

release and subsequent trouble-shooting, it has so far proven itself capable of tackling this particular problem. The multi-physics and optimization applications of the code have not been required, but both could justify further research.

The SU^2 solver is vertex-centered and based on finite-volume methods. In general, the following spatial discretization scheme has been successfully employed to attain convergence on a reasonable solution: starting with Roe 1st order (upwind scheme, first-order accurate in space) and then, once converged, restart utilizing Roe 2nd order (upwind scheme, second-order accurate spatially). Jameson-Schmidt-Turkel (JST) has been implemented successfully as well both with inviscid and viscous terms, and gradient computation has been done via the weighted Least-Squares method. The exception to this format was the flat plate example where the end solution was solved using the Lax-Friedrichs numerical integration.

From the perspective of temporal discretization, current runs have been steady-state and the lower-upper Symmetric-Gauss-Seidel (LU-SGS) iteration is being applied to solve the linear system of equations. The Courant-Friedrichs-Lewy (CFL) number has been set to four for most runs, and the solution becomes unstable unless this is ramped by a factor less than two. Cauchy convergence criteria have generally been used with an epsilon of 0.0001.

Grid Study

The general scheme of this project has been to build to the final scenario in three distinct steps: flat plate model with hemispherical VG, clean NACA-0012 airfoil at various angles of attack, and finally the same NACA-0012 airfoil with hemispherical VG. Time and computational resources permitting, a parametric study of multiple configurations of hemispherical VGs on the airfoil would be desirable. Mesh resolution in the vicinity of the viscous surfaces has been a challenge, particularly concerning the grid buildup around the VGs. There have

also been some issues with the SU^2 mesh decomposition code and running the solutions via the Kraken system, so efforts were made to reduce mesh cell count wherever possible.

As a means to isolate the effect of the hemispherical VG and study the flow around it, the first simulation was created with a flat plate in a channel-type flow scenario. The grid was created via the PointWise T-Rex functionality, and the total size was 582,070 cells; making it manageable for solutions on a home computer. From a resolution standpoint the overall mesh size was sufficient, but more time could be spent redistributing the existing cells towards the plate surface and away from the far-field; see Figure 13 [25].

The next step was to effectively grid up a NACA-0012 airfoil, first without the VGs and then with them added. So far in the project, only the bare airfoil has been completed. It is reasonable to suspect that the mesh-generation for the airfoil with VGs will be a challenge, but some important lessons have already been learned in preparation for that next step. The bare airfoil mesh consists of 6.7 million cells which makes it difficult to solve without more processing power than available in a home computer. This grid was also created via PointWise and the T-Rex function, and it too could use a redistribution of cell density to better reflect the anticipated gradients in the flow, see Figure 14 [25].

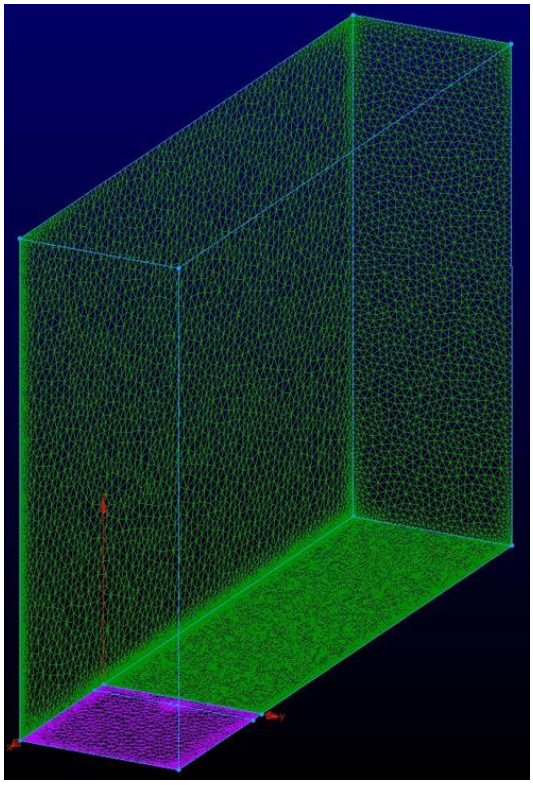

Figure 13. Flat plate mesh [25].

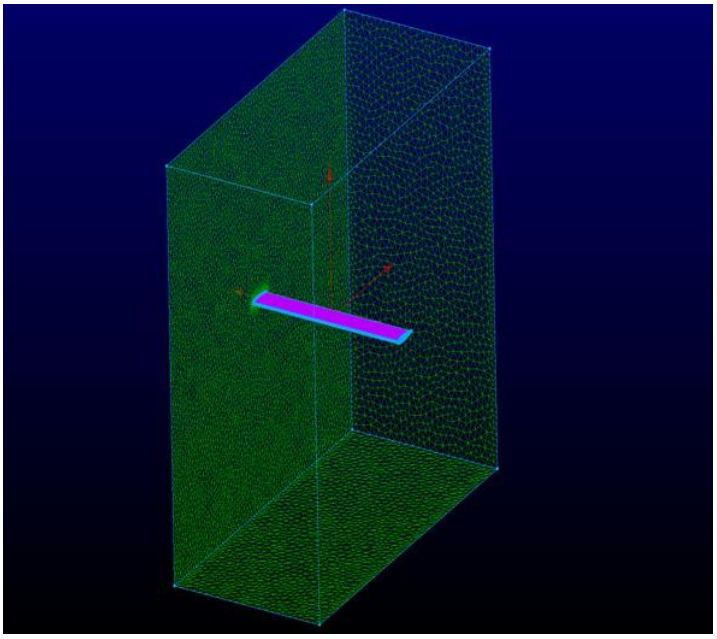

Figure 14. Airfoil mesh [25].

Experimental Setup

Water Tunnel

The UTSI water tunnel is a closed-circuit, continuous flow horizontal design. It is driven by a 14 pitch, 4 blade propeller in a 12 inch pipe between the upstream and downstream reservoirs. As shown in Figure 15 the test section is enclosed on three sides by Plexiglas and the top surface is free. The free surface is necessary for access to models, but a sheet of Plexiglas had to be installed so that the laser sheet was not distorted by hitting surface waves. The test section is 15 inches wide, 60 inches long and has a maximum depth of 18 inches.

The support apparatus for the airfoil was setup on rails fitted to the top of the test section. It allowed for consistent x and z placement of the airfoil, with about 1/4 inch of clearance in the y axis.

Two dye injection probes were used primarily for the final portion of testing; they were both one-exit probes but one was larger and allowed more dye to flow, while the other was smaller and could be easily moved over the surface of the airfoil. The smaller probe was used to detect separation on the surface and the larger probe was used for the actual image collection. Positioning of the larger probe was critical to reducing free stream disturbance, so it was twisted and dipped such that only the very exit was in line with the laser sheet. The exit pressure was throttled down from five pounds per square inch to match the free stream velocity and minimize induced flow.

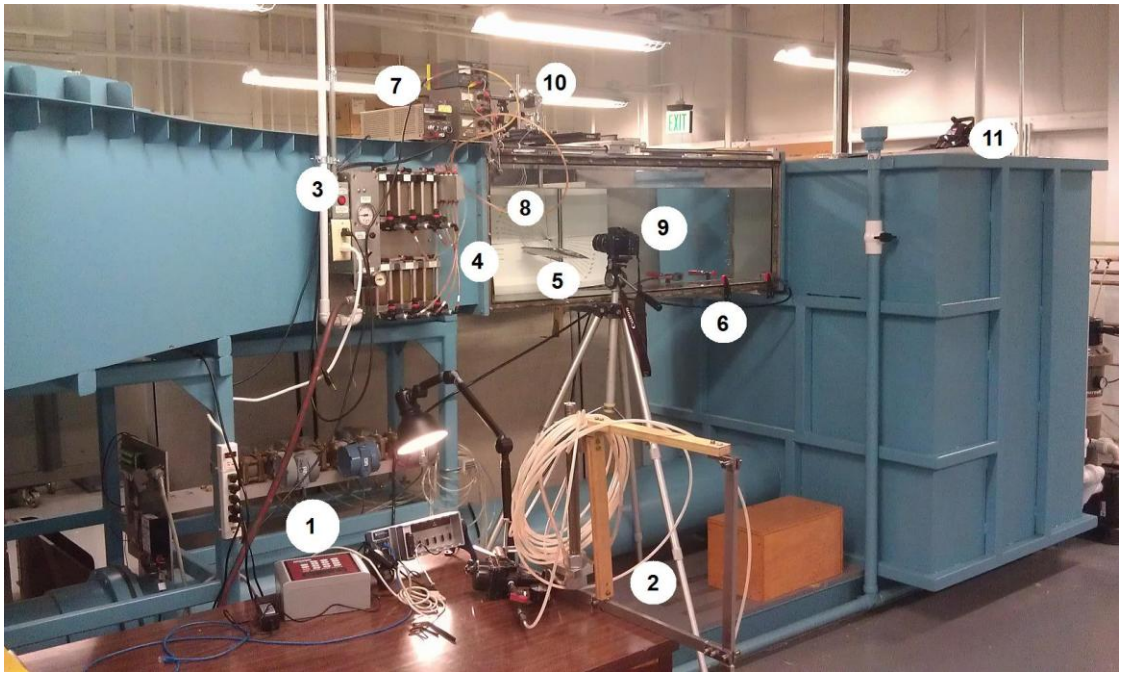

Figure 15. Setup at water tunnel; 1) flow meter controller, 2) camera tripod mounts (marked for consistent placement), 3) shop air pressure regulator for dye injection, 4) dye tanks, 5) NACA-0012 airfoil model, 6) flow meter sensors, 7) power supply controllers for three forward-mounted lasers and rotating mirror prism, 8) inclinometer for angle of attack measurements, 9) Canon Rebel T1i EOS digital SLR camera, 10) three forward-mounted lasers and rotating mirror prism mount, and 11) fourth laser (not shown) and power supply.

Model

The airfoil model is a NACA-0012 with a 7 inch chord and 12 inch span; streamlined at the tip while the root is open for the passage of the support strut and any piping to the tapped holes in the surface. Chord wise columns of taps are drilled into the upper and lower surfaces of the airfoil for pressure measurement or, in this case, dye injection. The airfoil connects to the external support apparatus via an adapter block that was designed and fabricated for this experiment. This block mates the span wise support rod to the adjustable stinger at the base of the tanks support apparatus. Notably this support setup allows for

a range of negative 20 to positive 30 degrees angle of attack. Some climbing/descending trials were attempted but the adjustment on the support did not allow for rapid changes to the angle of attack; nor were they uniform in rate.

The vortex generation was provided via three different sizes of Glamour GLITZ^{TM} Hot Fix Crystals (pearl rhinestones). Figure 16 shows the relative sizes; diameters of 0.154, 0.197, and 0.311 inches. They worked out very well; easy to glue onto the surface and then pick off after for relatively quick changes between configurations. They were placed accurately via the 2 inch by 2 inch grid stenciled onto both upper and lower surfaces of the airfoil; see Figure 17. Each grid square is 1/8 inch of span and 1/8 inch of chord. As evident in Figures 18 and 20, a glossy white strip of tape was placed down the center of the airfoil in order to reflect the laser sheet back up so that the dye was further illuminated.

Figure 16. Three hemispherical vortex generators, against a scale in inches.

Figure 17. Airfoil model marked with 1/8" spaced lines and grid pattern.

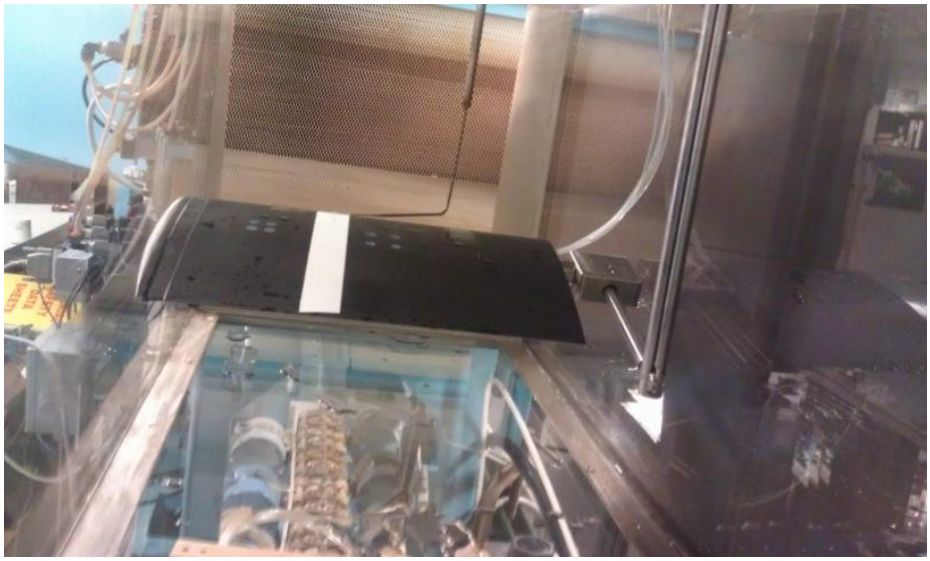

Figure 18. Top view of airfoil and dye probe, from downstream looking upstream. Dye probe is angled to reduce downstream flow disturbances.

Figure 19. Example configuration; medium VGs with spacing factor of 1.2.

Flow Visualization

The key to success or failure with this study was the quality of imagery. There were many inputs to the end product, including: laser power/beam-width, dye density, ambient light in the lab, turbulence in the tunnel, smoothness of the

airfoil surface, vibrations from the pump, standing waves on the water surface, alignment of the lasers, camera settings, and lens limitations.

Essentially the setup was to enable a system of four lasers to strike the bottom of a rotating mirror-prism and create a 2D or quasi-3D sheet of laser light to illuminate the fluorescent dye that was being injected upstream of the airfoil. Images of this dye stream reacting to the modified flow field around the VGs on the airfoil then provided an understanding as to how the VGs would change the overall flow separation point. The quasi-3D portion is due to the fact that each of the lasers had a different beam-width, and this fact was taken advantage of so that the flow could be visualized within a finite width; about the width of the largest VG. This meant that the airfoil didn't need much shifting in the y axis in order to see the flow from one side of the VGs to the other.

Table 1 shows the camera settings that were used throughout the experiment process; notably the still photos did not achieve enough quality to be used to measure separation point. In the final analysis, videos were taken which were then submitted to post-processing to generate usable still images. Figure 20 shows a still collected from video before processing by the MATLAB script attached in appendix A. Figure 21 shows the post-processing result, and Figure 22 is an enhancement of that photo showing the grid points. In order to determine separation the pixels were counted for several different stills of the same configuration; the results of this process will follow.

Table 1. Camera settings for optimal imagery.

Setting	Manual	Program	Video
ISO	320	Auto	Auto
Shutter Speed	2.0	Auto	Auto
Aperture Value	2.2	Auto	Auto
Resolution	2240 x 1680 pixels	2240 x 1680 pixels	1280 x 720 pixels
Zoom	Maximum Wide	Maximum Wide	Maximum Wide
Sharpness	High	High	High
Contrast	High	High	High

Figure 20. Still collected from video footage of clean airfoil configuration at 15^{o} angle of attack.

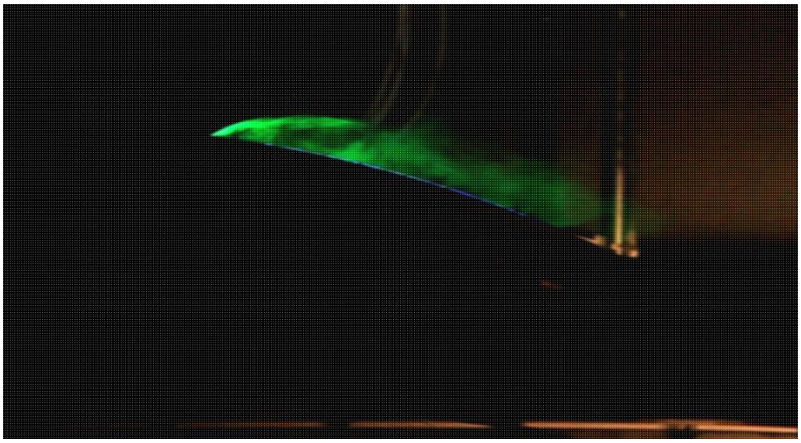

Figure 21. Grid overlay after MATLAB processing.

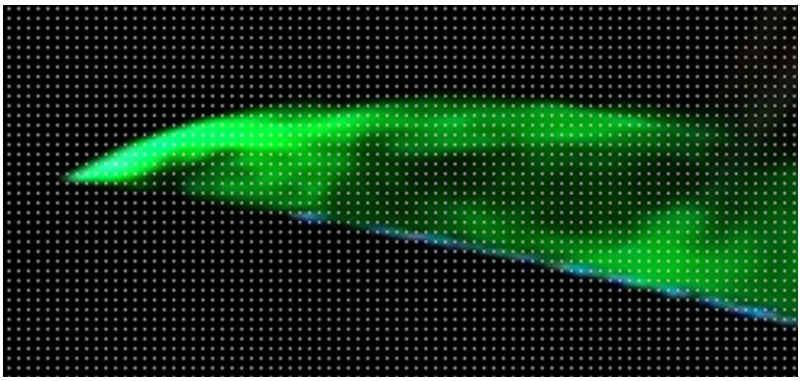

Figure 22. Enhanced view of Figure 21.

Equipment

In order to standardize the flow speed through the test section, both the power setting on the pump and an ultrasonic flow meter were used. The pump setting was left unchanged, but the indicated flow speed would vary with angle of attack. The Innova-Sonic™ Model 205 indicated anywhere from 0.99 to 1.12 feet per second of flow for all angles of attack. For 15 degrees that speed was generally 1.04 feet per second. When utilizing the calibration (Figure 49 in appendix B) for this setup, this means a local free stream speed for the airfoil of 0.88 feet per second. This is acceptably close to the theoretically-determined speed of 0.91 feet per second that would give a Reynolds number of 50,000.

There were two cameras used in these experiments; the first was the Cannon Rebel T1i previously mentioned and the second was an older-model Olympus CAMEDIA E-10. Although the Cannon was newer and had much greater resolution (15.1 megapixel), the Olympus (4 megapixel) was initially used due to its wider lens. This lens allowed for a smaller f-stop value which meant shorter exposure times and less image blur. In the end, however, the Cannon was used to capture video since the Olympus did not have video capability.

Test Variables

Although a range of angles of attack were measured from 10 to 20 degrees in 2.5 degree increments, 15 degrees was found to be the most illustrative of the effects of the VGs. As illustrated by Figures 23 and 24 12.5 degrees has separation after the leading edge that re-attaches downstream. The lowest angle of attack that demonstrated full separation without a leading edge separation bubble was chosen so that any improvement could be immediately visible.

Figure 23. Still collected from video footage of clean airfoil configuration at 12.5^{o} angle of attack. Re-attachment occurs just forward of the probe showing the trailing edge of the laminar separation bubble.

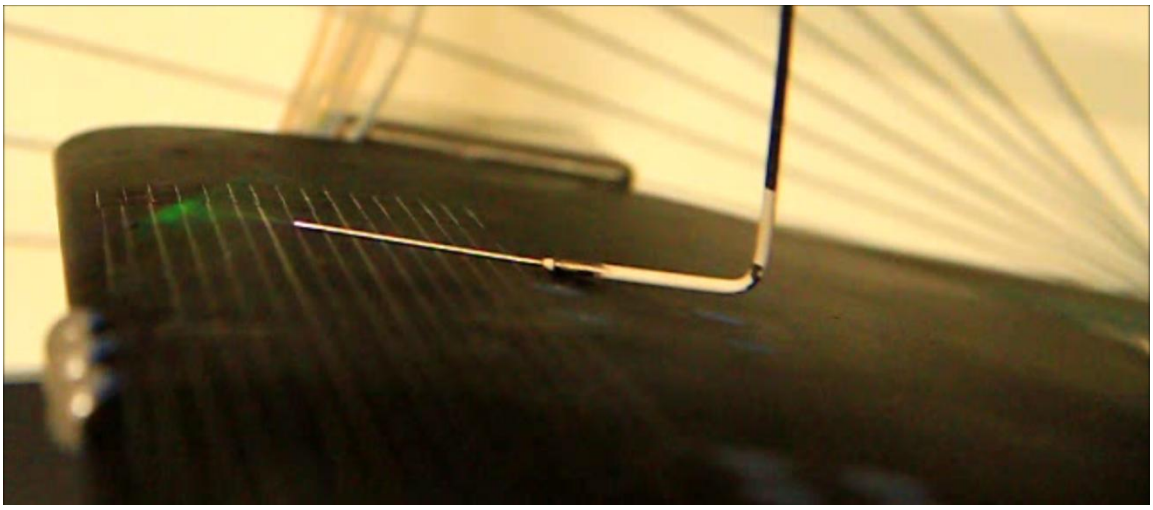

Figure 24. Still collected from video footage of clean airfoil configuration at 12.5^{o} angle of attack. Separation at leading edge of laminar separation bubble.

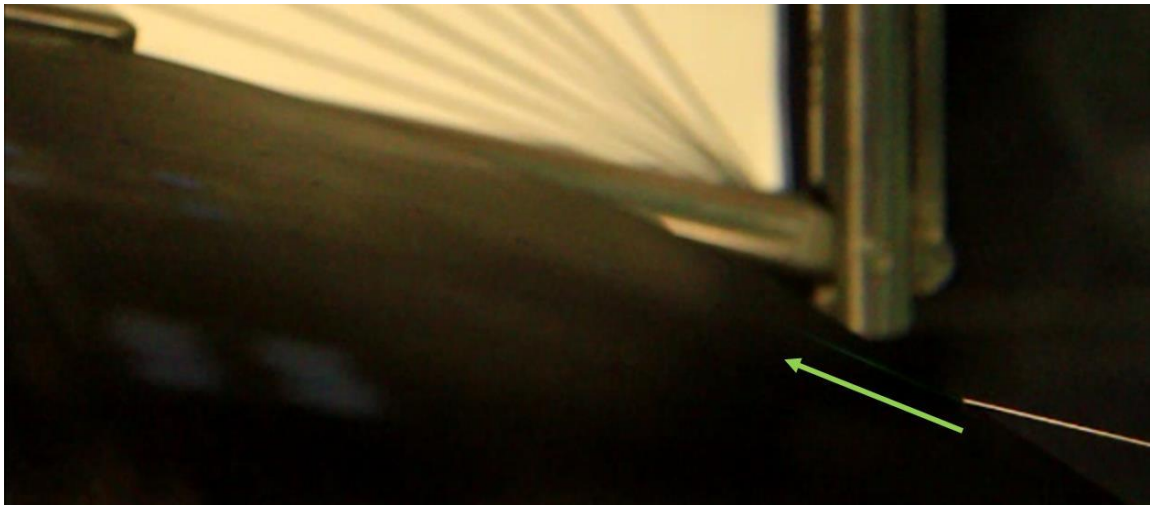

Figure 25. Still collected from video footage of clean airfoil configuration at 15^{o} angle of attack. Recirculating flow from trailing edge illustrates full leading edge separation without re-attachment.

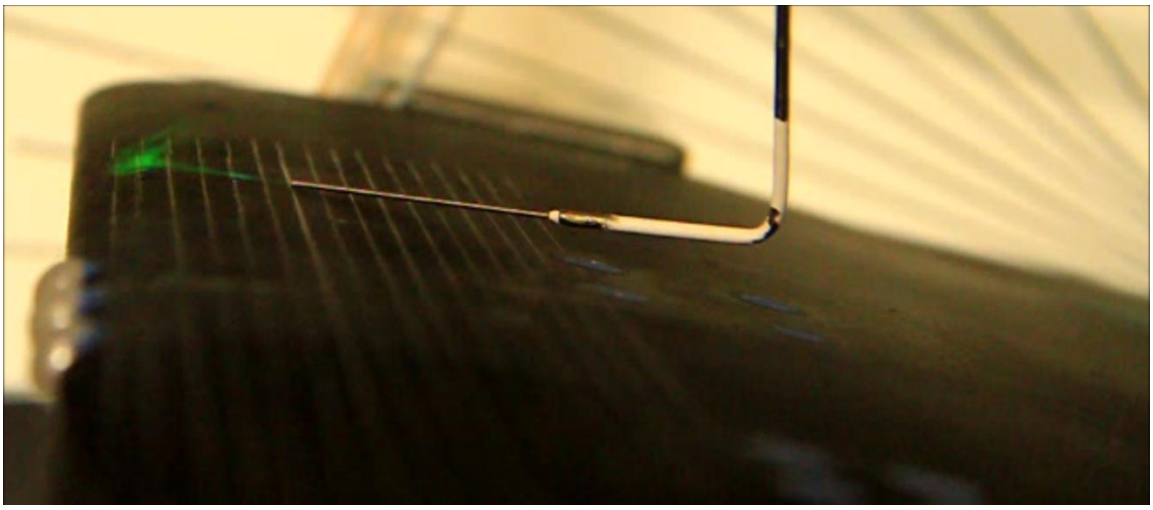

Figure 26. Still collected from video footage of clean airfoil configuration at 15^{o} angle of attack. Leading edge separation demonstrated over clean portion of airfoil.

Figures 25 and 26 demonstrate the characteristic being sought; recirculating flow right at the trailing edge that continues up until the leading edge separation. This was the case for the non-VG portion of the airfoil at 15 degrees angle of attack, and is why this angle was picked to compare all configurations.

The Reynolds number was chosen to be $5x10^{4}$ for two reasons: the water tunnel has known problems with standing waves past one foot per second [26], and $5x10^{4}$ is the lowest justifiable range for helicopter flight in the region of the retreating blade; where dynamic stall becomes a problem. This Re also corresponds to smaller Unmanned Air Vehicle wings.

The vortex generators themselves were part of a pearl rhinestone kit which had an excellent uniformity of manufacture. The sizes, therefore, were pre-determined and worked out to a suitable range. The spacing was varied within a 2 inch grid along the leading edge of the airfoil most visible in Figure 17. The heights of the VGs were slightly smaller than the radius by 0.005"; making the VGs within 97% of a perfect hemisphere.

CHAPTER IV
RESULTS AND DISCUSSION

Simulation Results

Flat Plate Study

The flat plate with VG study was completed using the Lax-Friedrichs numerical method, which is second-order accurate in space and sufficient for this laminar investigation. Although the S-A turbulence model was attempted, more success was achieved while keeping the flow laminar, and the max Reynolds number below 2.3 million. The Mach number was 0.2, and the flow passed over the plate at zero angle of attack. Convergence was reached in fewer than 400 iterations using the Cauchy criteria as mentioned above. See Figure 27 [25] for a close-up of the grid resolution for the VG and Figure 28 [25] for post-processing imagery. The streamlines moving past the hemisphere illustrate how far out from the VG these disturbances propagate, and also show where the vorticity is being generated in displacing the free stream fluid.

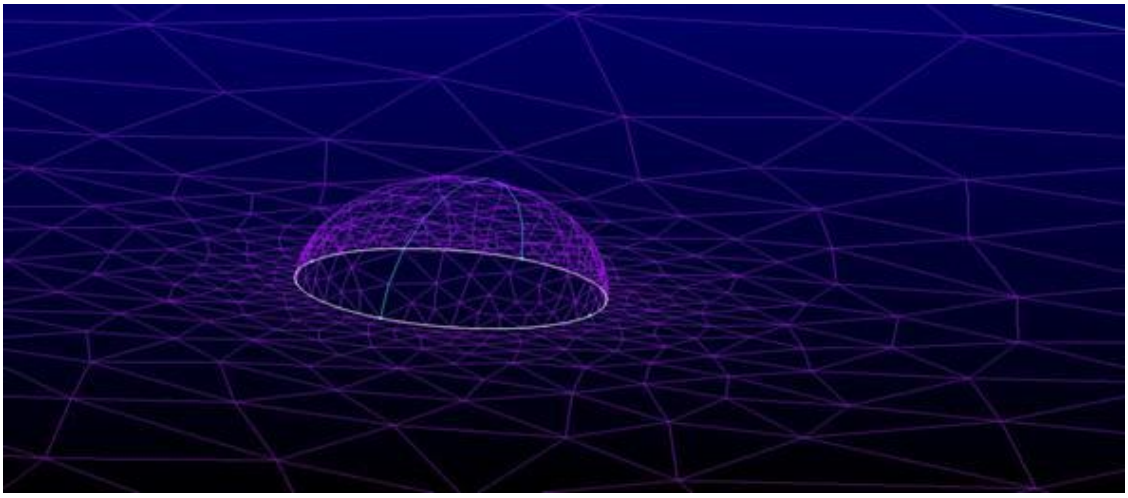

Figure 27. VG mesh over flat plate [25].

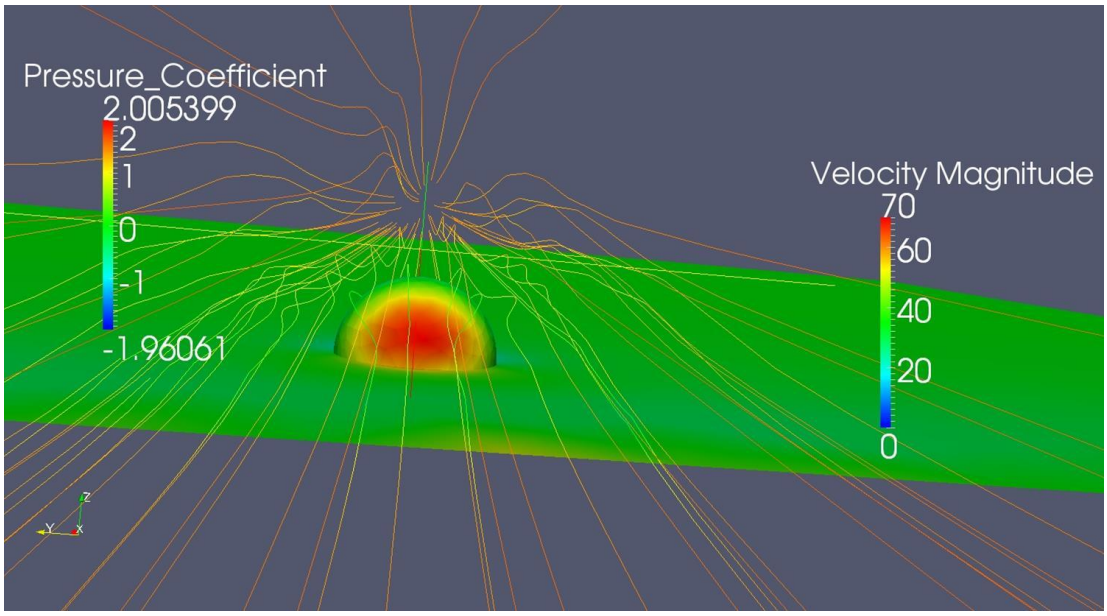

Figure 28. Simulated flow around a VG on a flat plate [25].

Clean NACA-0012 Airfoil

Simulations of the NACA-0012 airfoil have been completed with the 2nd order Roe numerical scheme with both turbulent and laminar flow for comparison. The Reynolds number has been computed to approximately 150,000 for all the runs, including angles of attack from zero to twenty-five degrees. Once the solution converged at zero degrees angle of attack, copies were made of that restart file and multiple runs began. Some issues with memory-handling internal to the SU^2 code made this process take a bit more time than otherwise necessary, but after numerous restart files the solutions were all converging rapidly.

Unfortunately, some additional complications with the output from SU^2 mean that currently available data cannot be easily visualized. More work is required in order to achieve functional post-processing of the simulations. In lieu of adequate visualization of the flow there is a comparison below of the shape of the lift-curve slopes and lift to drag ratios generated by the simulations (Figures

29 and 30 [25]) of the turbulent and laminar simulations respectively. From a rough comparison to experimental results (Figure 31 [27]) one can conclude that the data being produced seems to illustrate a reasonable trend. Notably, the experimental data was collected at Reynolds number of $2x10^4$.

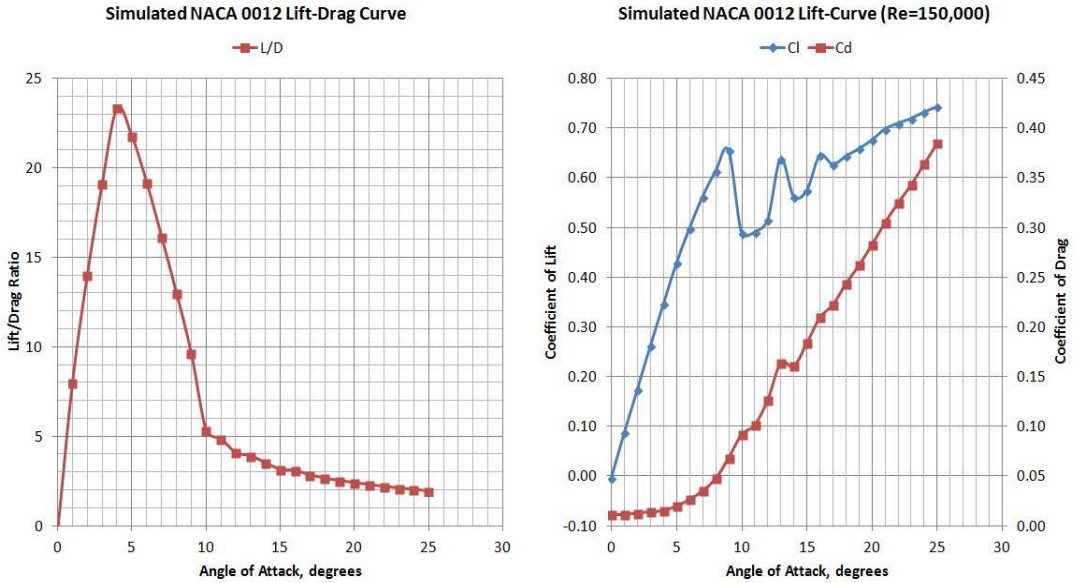

Figure 29. Turbulent simulated NACA-0012 data [25].

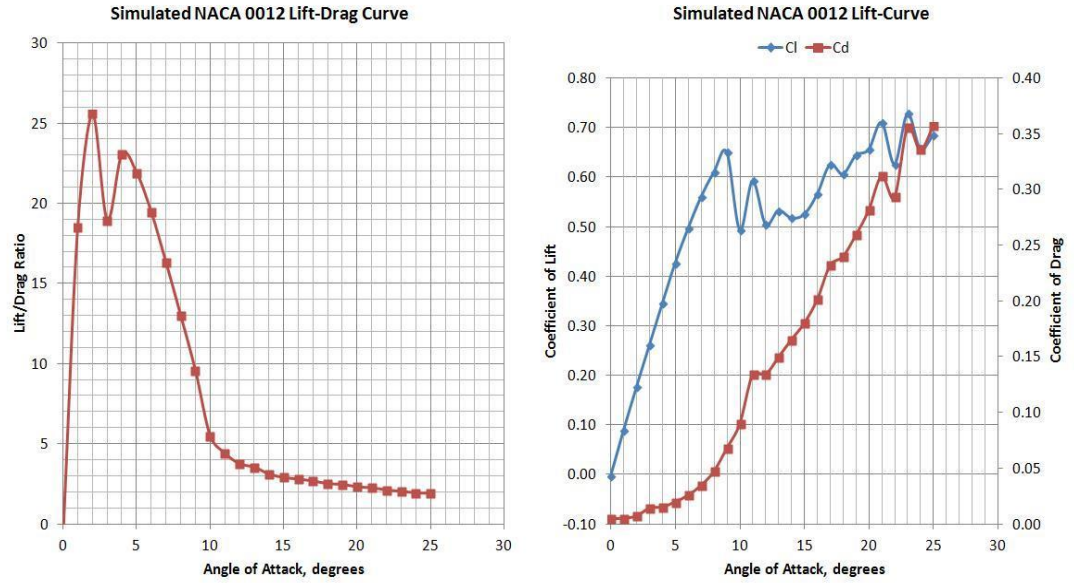

Figure 30. Laminar simulated NACA-0012 data [25].

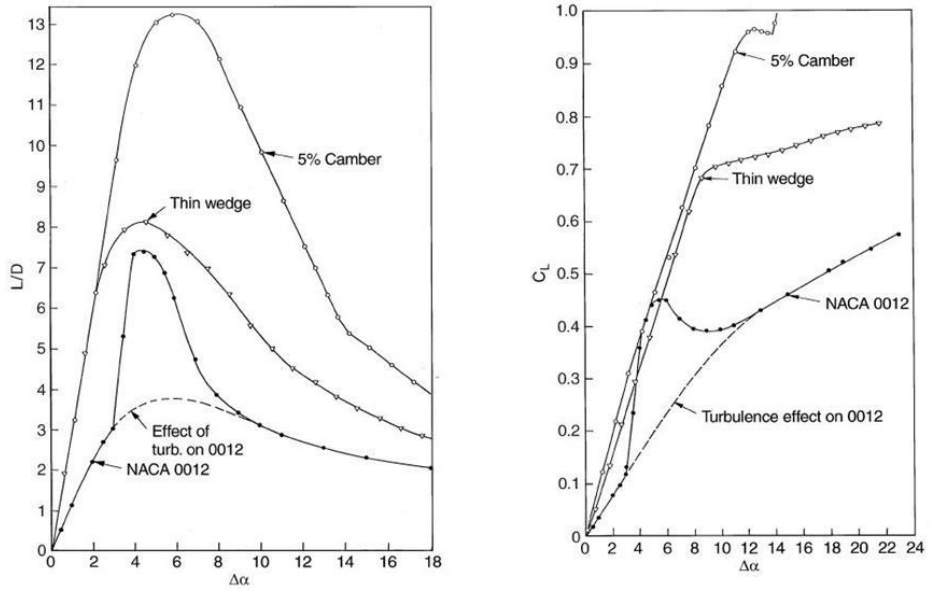

Figure 31. Experimental NACA-0012 data [27].

NACA-0012 with VG

These results were not collected as time was not available for continued simulations. This is recommended follow-on work.

Experimental Results

After image processing, the pixels were counted to each separation point and the results tallied in Table 2. Although there was no quantitative measurement possible for the actual horseshoe vortex, it was captured clearly for several of the configurations. One of these is illustrated in Figure 32 below. Additional figures depicting the side view of the various 15 degree configurations are available in appendix B.

Table 2. Matrix of configurations and subsequent separation measurements for 15 degrees angle of attack.

Horizontal Distance to Separation						
Configuration			# Grid Points	# Pixels	Inches	Sep/chord x/c
Size	D (inches)	y/D				
Clean	N/A	1.0	9.00	36	0.3000	0.0427
Large	0.3110	1.2	14.50	58	0.4833	0.0687
		1.6	16.00	64	0.5333	0.0759
		3.2	23.00	92	0.7667	0.1090
Medium	0.1969	1.2	7.50	30	0.2500	0.0356
		1.6	11.25	45	0.3750	0.0533
		3.2	19.00	76	0.6333	0.0901
Small	0.1535	1.2	24.00	96	0.8000	0.1138
		1.6	14.00	56	0.4667	0.0664
		3.2	14.25	57	0.4750	0.0676

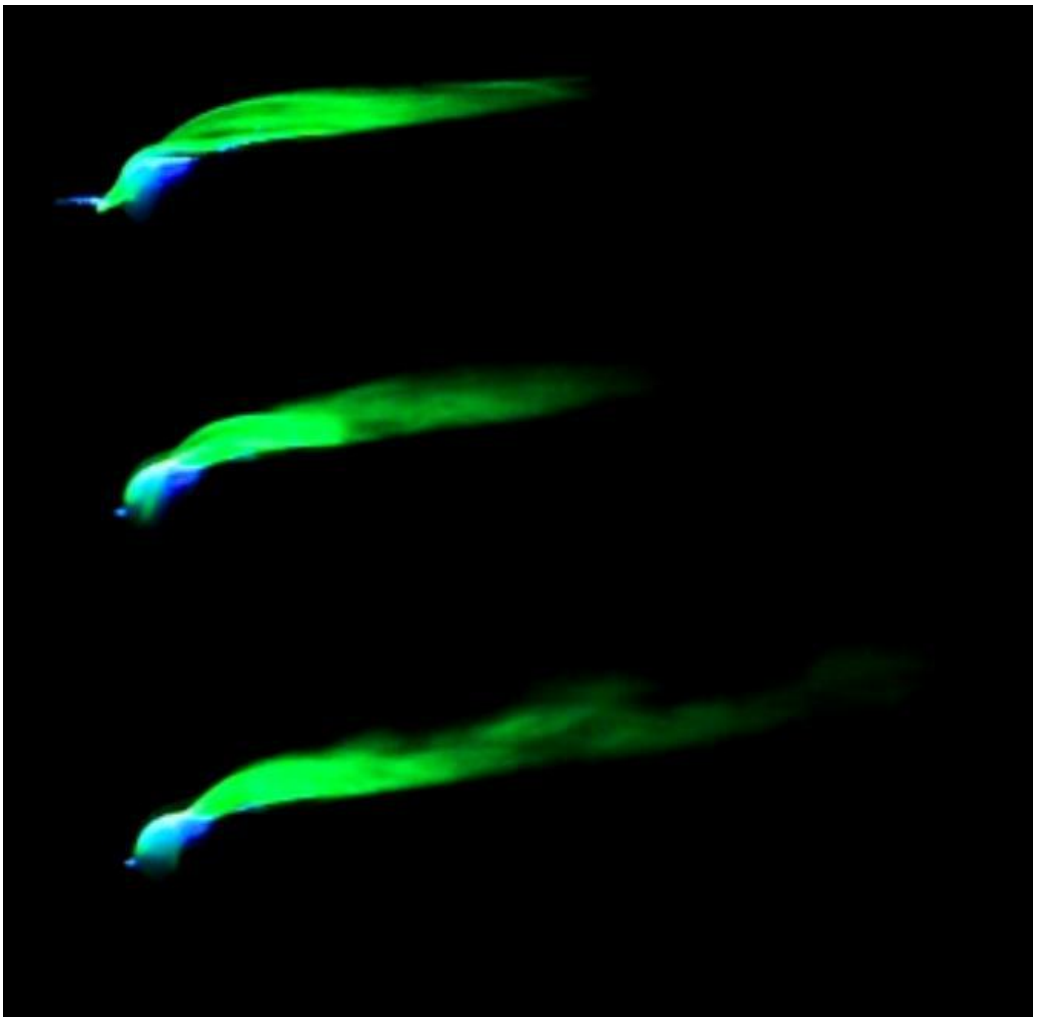

Figure 32. Three close-ups of the medium VG configuration at 15^{o} angle of attack and a spacing factor of 3.2. The primary horseshoe vortex and trailing vortices are clearly visible.

Error Analysis

The process by which the quantitative data were collected has some ambiguity. By standardizing the placement of the airfoil in the tunnel, the angle of attack indicator, and the camera tripod legs the author believes that any significant parallax has been effectively removed. Likewise turbulence intensity, motor vibrations, and wall boundary layer effects of the tunnel itself would all apply equally to each configuration at a particular angle of attack. The dye was

mixed to the same proportions for each refill to ensure a change in density wouldn't interfere with data.

The most significant source of uncertainty is the interpretation of the images themselves. For this reason the mean separation point would be chosen from slow motion analysis of the video via Windows Movie Maker. This data point would be the central point used, and then fluctuations would be counted out as either greater or less than that mean. These are the error bars shown on the previous graphs. This process is also tabulated at Table 3. The final error applied to the preceding graphs was due to the resolution of the gridlines on the airfoil itself. With 1/8th inch lines in the span wise and chord wise directions, 1/16th inch was effectively resolved. The diameter measurements were carried out with a Vernier caliper that was accurate to a thousandth of an inch; any associated uncertainty in beyond the resolution of the spacing factor graphs.

Table 3. Uncertainty in separation measurements for 15 degrees angle of attack.

Uncertainty in Separation Calculations											Error Value		
Configuration			Min	Max	Min	Max	Min	Max	Min	Max	Min	Max	
Size	D (in)	y/D	Points	Points	Pixels	Pixels	Inches	Inches	x/c	x/c	x/c	x/c	STD-Dev
Clean	N/A	1.0	9.00	10.00	36	40	0.3000	0.3333	0.0427	0.0474	**0.000000**	**0.004741**	0.274%
Large	0.311	1.2	13.00	16.00	52	64	0.4333	0.5333	0.0616	0.0759	**0.007111**	**0.007111**	0.711%
		1.6	14.00	21.00	56	84	0.4667	0.7000	0.0664	0.0996	**0.009481**	**0.023704**	1.709%
		3.2	20.00	24.25	80	97	0.6667	0.8083	0.0948	0.1150	**0.014222**	**0.005926**	1.035%
Medium	0.197	1.2	6.50	13.25	26	53	0.2167	0.4417	0.0308	0.0628	**0.004741**	**0.027259**	1.727%
		1.6	9.00	13.50	36	54	0.3000	0.4500	0.0427	0.0640	**0.010667**	**0.010667**	1.067%
		3.2	18.00	20.00	72	80	0.6000	0.6667	0.0853	0.0948	**0.004741**	**0.004741**	0.474%
Small	0.154	1	22.00	24.50	88	98	0.7333	0.8167	0.1043	0.1161	**0.009481**	**0.002370**	0.627%
		1.6	10.75	15.00	43	60	0.3583	0.5000	0.0510	0.0711	**0.015407**	**0.004741**	1.053%
		3.2	11.00	17.50	44	70	0.3667	0.5833	0.0521	0.0830	**0.015407**	**0.015407**	1.541%

Size and Configuration Comparison

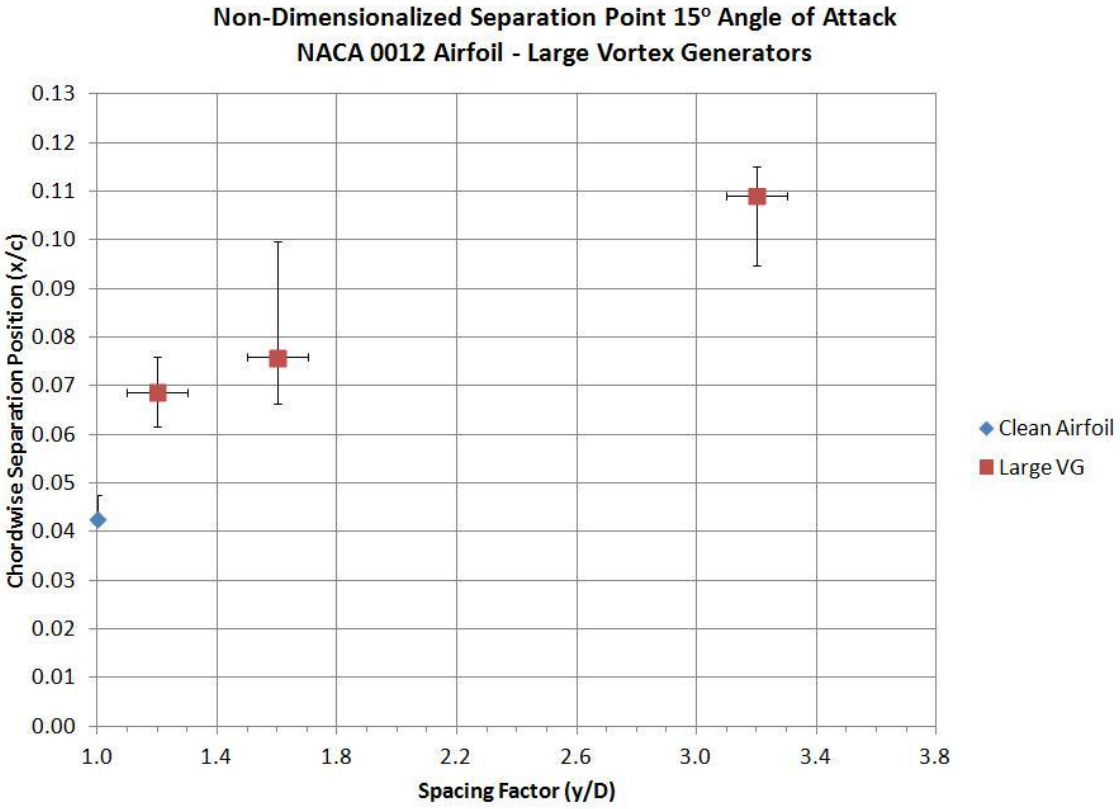

Figure 33. Separation point control effectiveness of large VGs at angle of attack of 15 degrees with error bars.

As depicted in Figure 33 there is an improving trend in effectiveness of the large VGs as the spacing increases. The associated error bars indicate some level of variability in the data points, but the trend is clear. Note that the data point at spacing factor 1.0 is the baseline clean airfoil. The large VGs as much as double the distance to flow separation when compared to the unmodified airfoil. Note that the spacing factor is the distance measured from center-VG to next center-VG divided by the diameter of that VG.

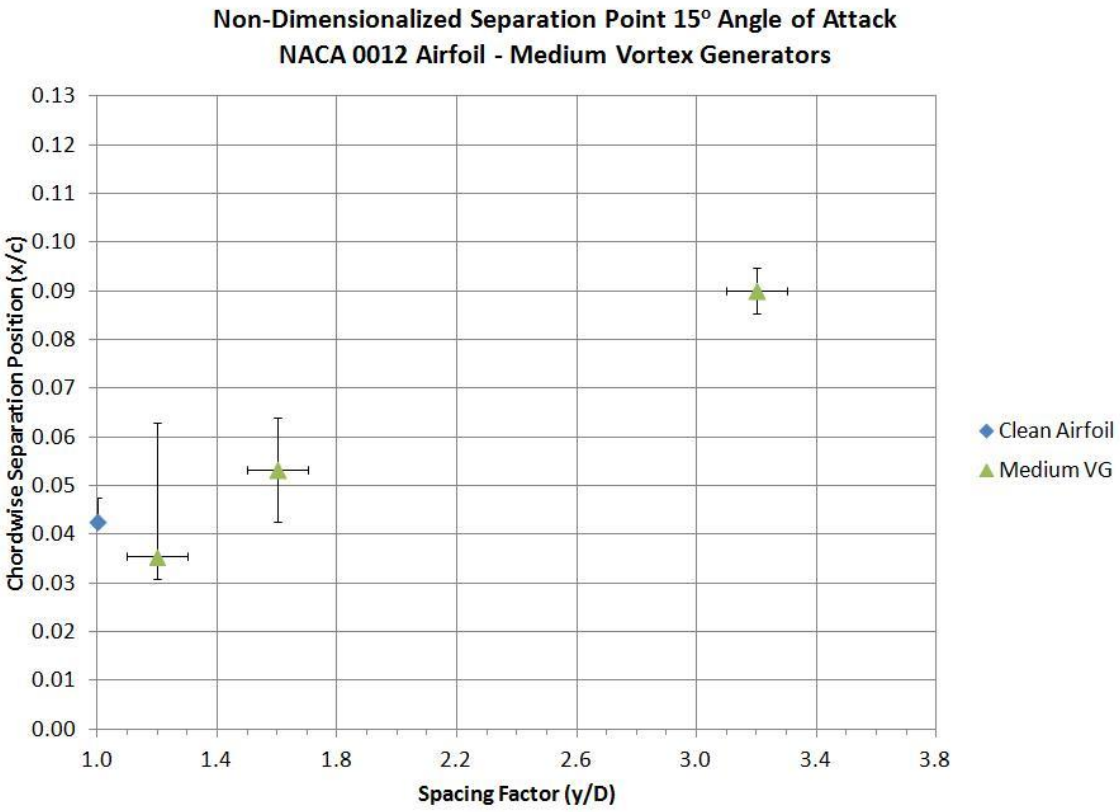

Figure 34. Separation point control effectiveness of medium VGs at angle of attack of 15 degrees with error bars.

As depicted in Figure 34 there is also an improving trend in effectiveness of the medium VGs as the spacing increases. The very first data point has a much larger potential for error, so it is possible that the apparent lack of effectiveness on separation delay is misleading. Multiple pictures were compared for that run and they confirmed the wide spread; meaning it could have been an inconsistent run. The last two spacing factors look like more usable data, but the first data point should be re-run to confirm whether the same trend exists for the medium VGs as was illustrated in the large VGs of Figure 33. Note that the data point at spacing factor 1.0 is the baseline clean airfoil. The medium VGs are still significantly delaying flow separation when compared to the unmodified airfoil.

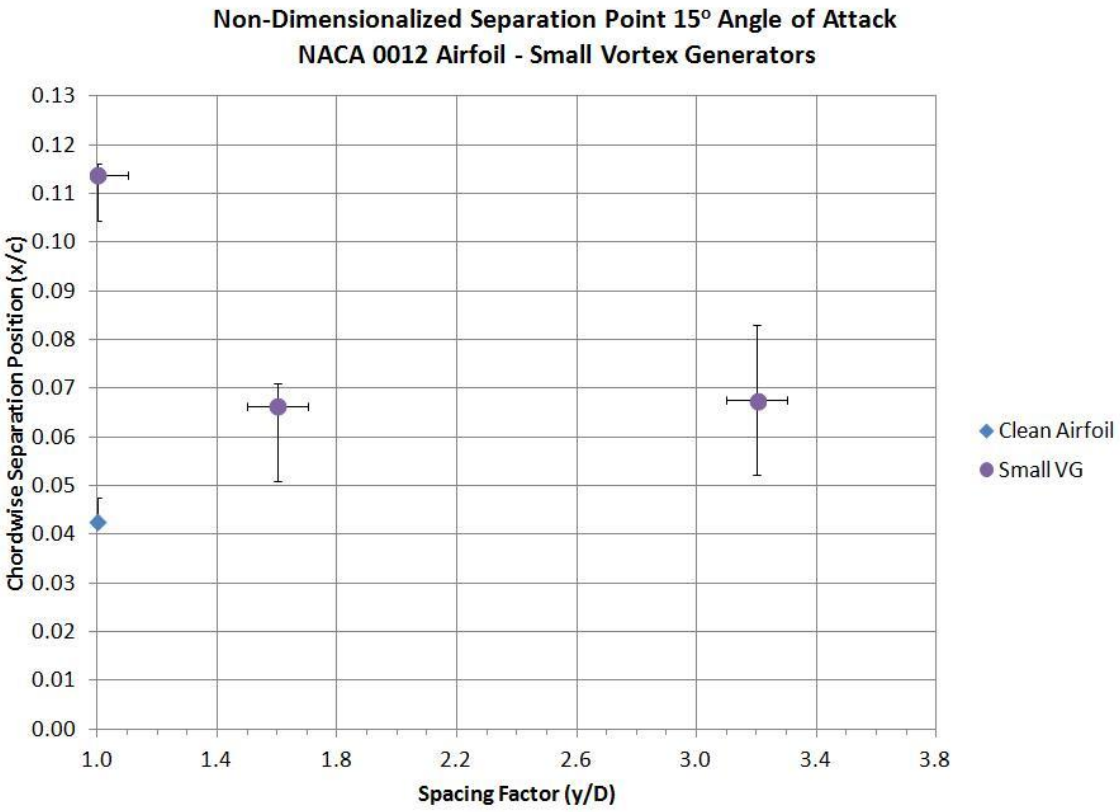

Figure 35. Separation point control effectiveness of small VGs at angle of attack of 15 degrees with error bars.

Figure 35, the small VGs, illustrates a significant change in trend as compared to the medium and large VGs. It should be noted that the first data point had the spacing so tight that the VGs were touching. Without a gap for the trailing vortices to form between adjacent VGs it is difficult to imagine the vortex dynamics. Evidently the overall effect is to increase the effectiveness at delaying flow separation for this configuration compared to any of the others. It is premature to hold this up as the example to follow since the same spacing factor for the medium and large VGs was not attempted. The second and third data points do not illustrate a very powerful effect on flow separation compared to the clean airfoil case at the far left. The error bars almost cover the range reaching to the separation of the clean configuration. This suggests that, aside from the

cumulative effect of pushing the small VGs together, they are too small to affect the flow to the same extent of the medium or large VGs.

Spacing and Configuration Comparison

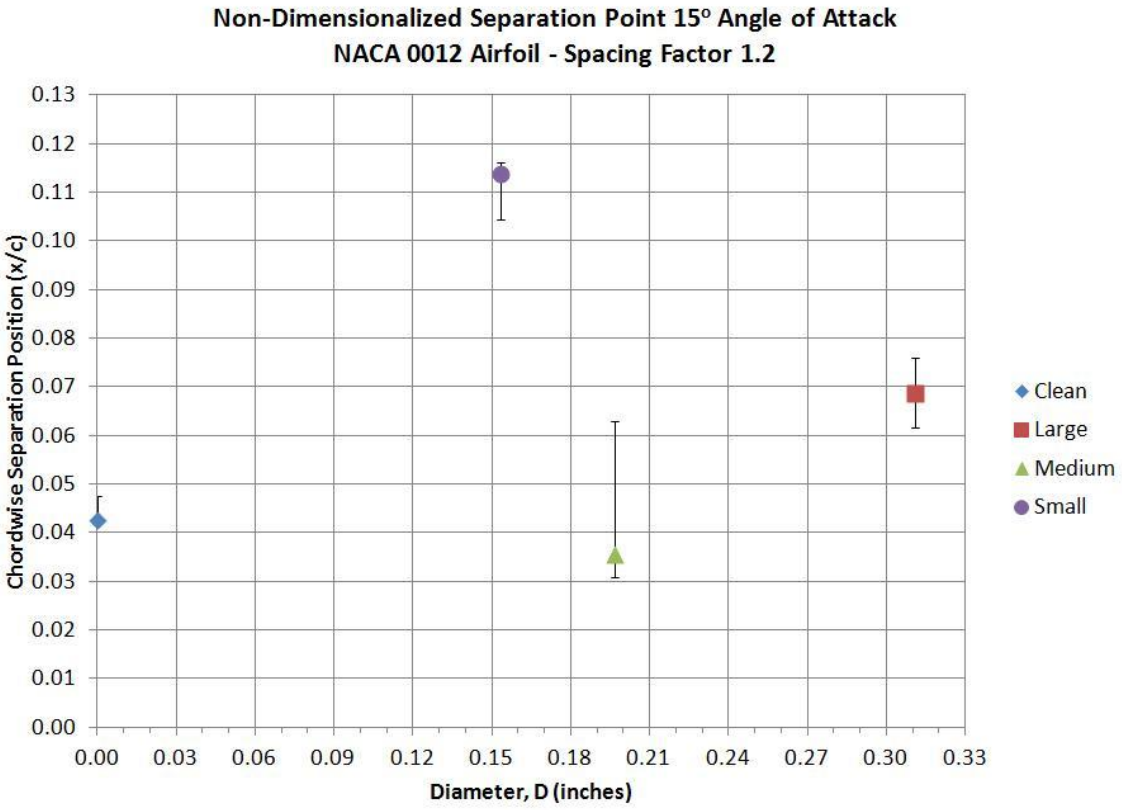

Figure 36. Separation point control effectiveness at angle of attack of 15 degrees with error bars for the VGs with a spacing factor of 1.2 except for the small VG which was mistakenly placed at a spacing factor of 1.0.

This graph illustrates the effectiveness of the VGs when compared head to head at a spacing factor of 1.2. In this case the small VGs are much more effective than either the medium or the large at delaying separation. Even given the medium VGs relatively wide spread of uncertainty, it is still less effective than the large VG, and in some cases counterproductive when compared to the clean airfoil configuration.

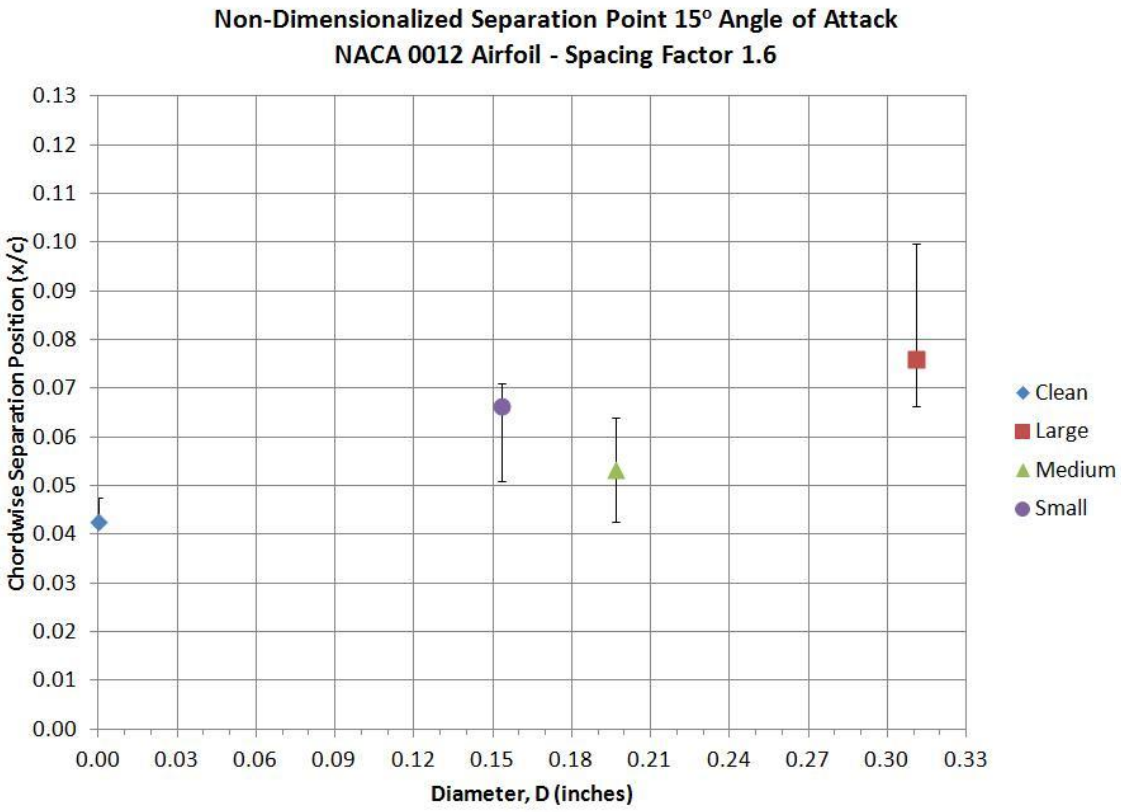

Figure 37. Separation point control effectiveness at angle of attack of 15 degrees with error bars for the VGs with a spacing factor of 1.6.

In Figure 37 the three sizes of VG are compared at a spacing factor of 1.6. In this instance, they are all much closer to each other but notably each improves the separation condition as compared to the clean airfoil. Here we see that the large VG has an advantage over the small, while the medium VG is still lagging behind both. All VGs show some potential effectiveness in delaying flow separation.

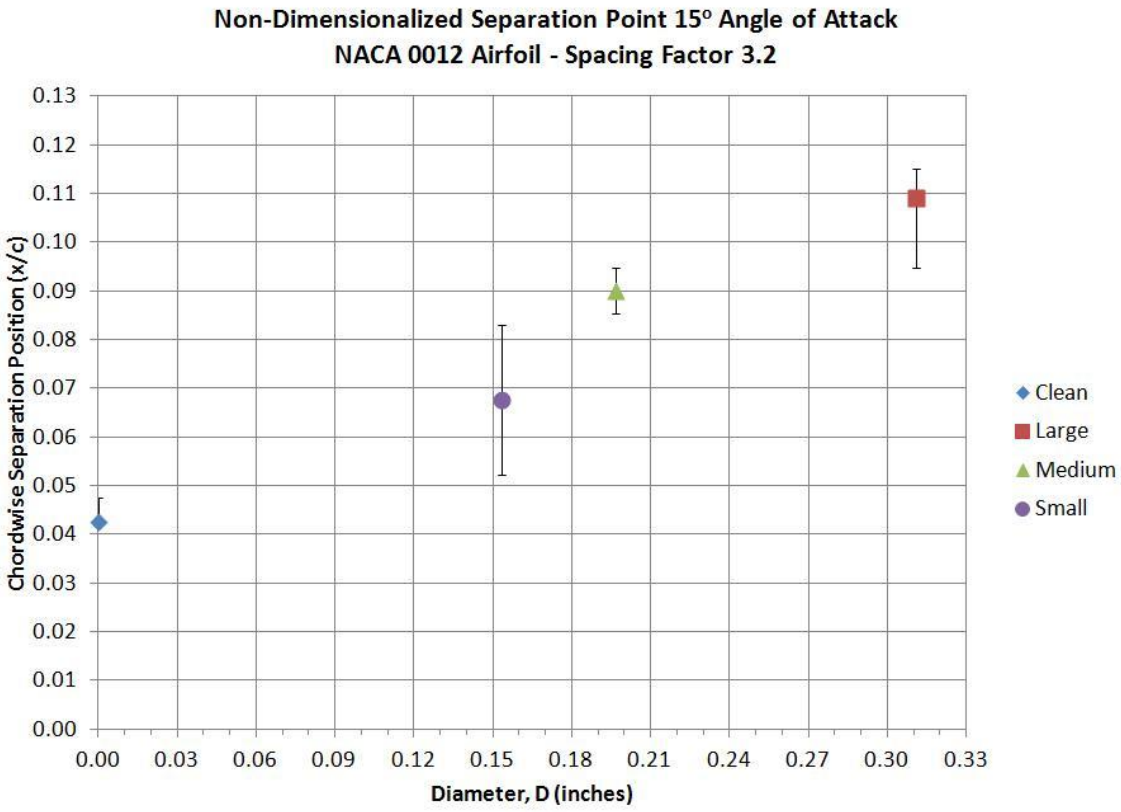

Figure 38. Separation point control effectiveness at angle of attack of 15 degrees with error bars for the VGs with a spacing factor of 3.2.

As the separation increases further the small VGs effectiveness has peaked, while the medium and large VGs are still improving. The large VG configuration is the most effective at the spacing factor of 3.2, followed fairly closely by that of the medium VG configuration. Figure 38 illustrates this effectiveness.

Effectiveness Limit Validation

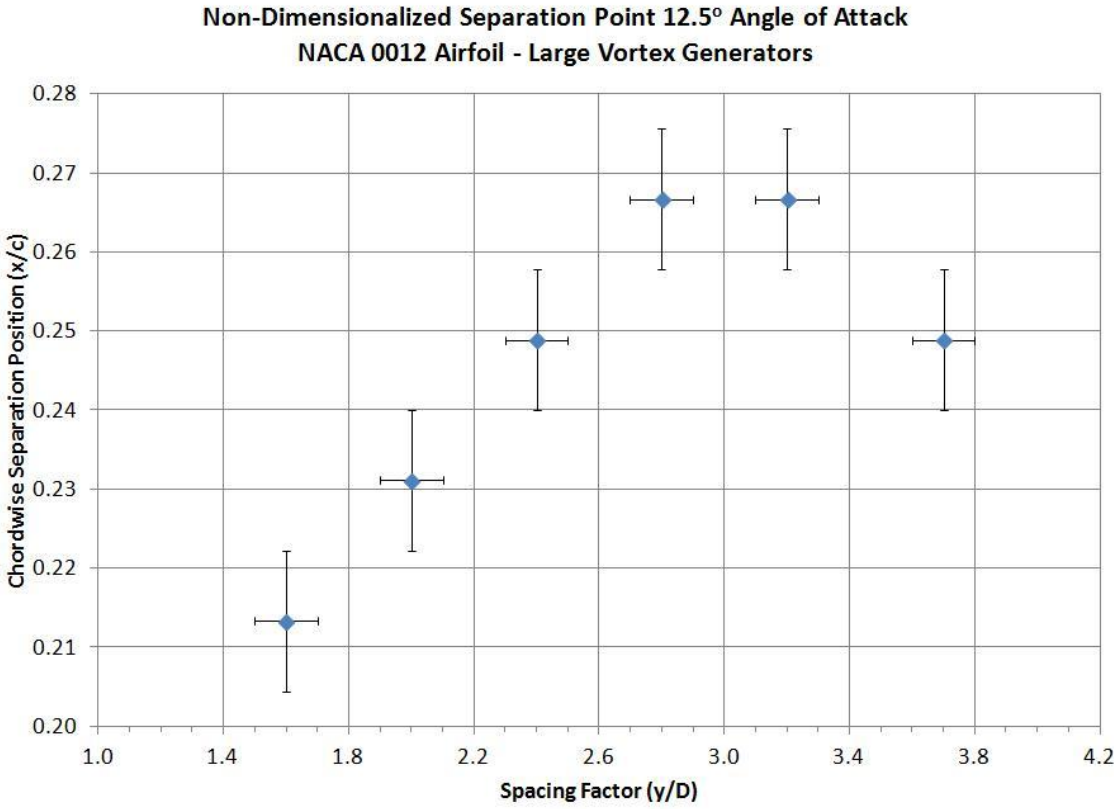

Figure 39. Span wise separation control effectiveness of large VGs at angle of attack of 12.5 degrees with error bars.

The large and medium vortex generator vs spacing factor plots indicate an apparently endless improving trend of separation effectiveness with increasing spacing. This is counterintuitive and the impression needed to be corrected by further data collection. There were two corrections required to the previous data: an expansion of the spacing factors and a validation of the imagery technique.

Figure 39 illustrates that the trend does decline after a particular maximum point at a spacing factor of approximately three. This data was gathered with regular lab lighting conditions by traversing the smallest dye probe in a span wise way across the surface of the airfoil. At particular chord fluid flow direction pattern

was noted and then compared upstream and downstream across the entire region being affected by the VGs on the leading edge. This trial was conducted at 12.5 degrees angle of attack because at 15 degrees the separation points were so close to the VGs as to make the dye difficult to observe.

Of note, 12.5 degrees had been the angle of attack where there was a laminar separation bubble between 5% chord and 43% chord as illustrated in Figures 23 and 24. This separation bubble was eliminated by the presence of the VGs at the leading edge.

CHAPTER V
CONCLUSIONS AND RECOMMENDATIONS

Conclusion

Vortex generators (VG), if located at the proper position can help reduce, minimize or possibly even eliminate flow separation over various airfoil profiles. The adverse pressure gradient caused by negative curvature can be acted upon by pairs of counter-rotating streamwise vortices; effectively mixing higher momentum flow from the external flow into the boundary layer. At Reynolds number of $5x10^4$ the separation point was investigated by using three different sized hemispherical VGs placed on a NACA-0012 airfoil in different configurations at a range of mid to high angles of attack. Naked eye observation in addition to laser-illumination of fluorescent dye was used to visualize the flow over the airfoil. The following results were attained:

1. The large VGs were most effective and had the most consistent correlation between separation delay and VG spacing. For an angle of attack of 12.5 degrees, tests showed that the optimum separation spacing between these VGs is about 3 diameters;
2. The medium VGs followed the same general trend, but had a significantly lower effectiveness all throughout the range of VG spacing; and
3. The small VGs mostly seemed inert in their interaction with the local flow, appearing stagnant except for the smallest spacing factor where the VGs were so close as to be in contact.

A numerical model of the baseline clean airfoil configuration was also developed for understanding of the fundamental flow events involved. The use of SU^2 code led to some issues, similar to that experienced by others since it is a newly developed code package. The major lesson in this research was the criticality of generating a good mesh. New releases of SU^2 are being published on an ongoing basis, but it seems that high quality results for cases like this

study are within reach. Efforts on this particular case will continue with SU^2, with the hopes of utilizing its optimization capabilities in later studies. The next step is adequately modeling the unsteady component of this flow and attaining high quality visualization to hone in on any vortical structures that can be developed.

Recommendations

The first recommendation is related to the outlier in the data collected thus far; the small VGs were mostly ineffective except for the configuration where the VGs were as close as possible. This illustrated an effect several magnitudes greater than the other two spacing for the same size VG, or even the rest of the VGs and spacing. In order to confirm this data, the same run should be repeated. After this, the medium and large VGs should be attempted with the same spacing constraint; the non-dimensionality would be lost between the three configurations, but the results might prove illustrative. In addition, each VG size should be run through the angles of attack for a single VG installed; this would illustrate the limits on how much each VG affects the flow of its neighbor.

Although this investigation has been based on the idea of using the dynamic similarity [28] of the flow in a water tunnel to make extrapolations for aerodynamic applications, it would be a good idea to have either Particle Image Velocimetry or Laser Doppler Velocimetry available. This would provide quantitative data about the flow field and any effects that may be hidden from the current setup. This would also provide a much better resolution of the dynamics of the trailing vortices behind the VGs, and allow for a prediction of their relative strength. Slices in the y-z plane could demonstrate the counter-rotating vortices and their distance to dissipation or any periodicity in their formation and dissipation.

Without much more equipment, a high speed color video camera capability would cut down significantly on the uncertainty in measuring

separation. Although the author has confidence in the range attained, and particularly the trends, it would be helpful to have a sharper image on which to rely. The airfoil is also already tapped for pressure measurement, so this would be useful information to compare with the numerical data; where pressure coefficients could be directly related.

Finally, a wake rake, to capture drag effects, would be a necessary addition in order to provide weight to the conclusions. There may be a high price to pay in terms of wake effects for the delays in separation point seen in this study. In closing, a parametric study such as this would benefit from many more configurations of sizes and spacing of VGs.

LIST OF REFERENCES

[1] O. Lögdberg, K. Angele and P. H. Alfredsson, "On the robustness of separation control by streamwise vortices," *European Journal of Mechanics-B/Fluids,* vol. 29, no. 1, pp. 9-17, 2010.

[2] F. M. White, Viscous Fluid Flow, 3rd ed., McGraw Hill, 2006, p. 67.

[3] P. B. S. Lissaman, "Low Reynolds Number Airfoils," *Annual Review of Fluid Mechanics,* vol. 15, pp. 223-239, 1983.

[4] J. A. K. Ackroyd, B. P. Axcell and A. I. Ruban, "L. Prandtl, in Verhandlungen des dritten internationalen Mathematiker-Kongresses in Heidelberg 1904, A. Krazer, ed., Teubner, Leipzig, Germany (1905), p. 484," in *Early Developments of Modern Aerodynamics*, Oxford, Butterworth-Heinemann, 2001, p. 77.

[5] K. M. Swift, "An Experimental Analysis of the Laminar Separation Bubble at Low Reynolds Numbers," The University of Tennessee Space Institute, Master's Thesis, Tullahoma, TN, 2009.

[6] H. Schlichting and K. Gersten, Boundary Layer Theory, 8 ed., Springer, 2000.

[7] I. Tani, "Low Speed Flows Involving Bubble Separations," *Progress in Aerospace Sciences,* vol. 5, pp. 70-103, 1964.

[8] T. J. Mueller and J. D. Delaurier, "Aerodynamics of Small Vehicles," *Annual Review of Fluid Mechanics,* vol. 35, pp. 89-111, 2003.

[9] H. D. Taylor, "The Elimination of Diffuser Separation by Vortex Generators," United Aircraft Corp., 1947.

[10] D. S. Miklosovic, M. M. Murray, L. E. Howle and F. E. Fish, "Leading-edge tubercles delay stall on humpback whale (Megaptera novaeangliae) flippers," *Physics of Fluids,* vol. 16, no. 5, pp. L39-L42, 2004.

[11] T. Cebeci and P. Bradshaw, Momentum Transfer in Boundary Layers, New York: McGraw-Hill, 1977.

[12] R. J. Pattenden, S. R. Turnock and X. Zhang, "Measurements of the flow over a low aspect-ratio cylinder mounted on a ground plane," *Experiments in Fluids,* vol. 39, pp. 10-21, 2005.

[13] T. Euler and J. Herget, "Controls on local scour and deposition induced by obstacles in fluvial environments," *Catena,* vol. 91, pp. 35-46, 2012.

[14] H. Werlé, "On the Flow of Fluids Made Visible," *Leonardo,* vol. 8, no. 4, pp. 329-331, 1975.

[15] H. Mai, G. Dietz, W. Geißler, K. Richter, J. Bosbach, H. Richard and K. de Groot, "Dynamic Stall Control by Leading Edge Vortex Generators," in *American Helicopter Society 62nd Annual Forum*, Phoenix, AZ, 2006.

[16] J. A. Ekaterinaris and M. F. Platzer, "Computational prediction of airfoil dynamic stall," *Progress in Aerospace Sciences,* vol. 33, no. 11-12, pp. 759-876, 1998.

[17] S. Ko and W. J. McCroskey, "Computations of unsteady separating flows over an oscillating airfoil," *AIAA Journal,* vol. 35, no. 7, pp. 1235-1238, 1997.

[18] G. Dietz, W. Geißler and H. Mai, "Auftriebsfläche mit verbessertem Ablöseverhalten bei stark veränderlichem Anstellwinkel". Germany Patent DE102005018427.8, 2005.

[19] G. Joubert, A. Le Pape, B. Heine and S. Huberson, "Vortical Interactions Behind Deployable Vortex Generator for Airfoil Static Stall Control," *AIAA Journal,* vol. 51, no. 1, pp. 240-252, 2013.

[20] J. Favier, A. Pinelli and U. Piomelli, "Control of the Separated Flow Around an Airfoil Using a Wavy Leading Edge Inspired by Humpback Whale Flippers," *Comptes Rendus Mecaniques,* vol. 340, no. 1-2, pp. 107-114, 2012.

[21] J. Lin, "Review of Research on Low-Profile Vortex Generators to Control Boundary-Layer Separation," *Progress in Aerospace Sciences,* vol. 38, no. 4-5, pp. 389-420, 2002.

[22] G. Mohamed, "Questions in Fluid Mechanics," *Journal of Fluids Engineering,* vol. 117, p. 3, 1995.

[23] R. H. Pletcher, J. C. Tannehill and D. A. Anderson, Computational Fluid Mechanics and Heat Transfer, CRC Press, 2010, pp. 272-276.

[24] F. Palacios, M. Colonno, A. C. Aranake, A. Campos, S. R. Copeland, T. D. Economon and e. al, "Stanford University Unstructured (SU2): An open-source integrated computational environment for multi-physics simulation and design," in *51st AIAA Aerospace Sciences Meeting*, 2013.

[25] D. R. J. Tucker, "Leading Edge Vortex Generation by Hemispherical Disturbance Generators," University of Tennessee Space Institute, Computational Fluid Dynamics Class Project, Tullahoma, TN, 2013 (unpublished).

[26] W. R. Michalchuk, "An Investigation of Different Golf Ball Dimple Flow Fields," The University of Tennessee Space Institute, Master's Thesis, Tullahoma, TN, 2006.

[27] F. W. Schmitz, "Aerodynamics of the model airplane," Redstone arsenal translation, 1967.

[28] D. M. McDaniels, "Background and Theoretical Considerations for Utilizing Water Tunnel Flow Visualization," The University of Tennesse Space Institute, Master's Thesis, Tullahoma, TN, 1986.

[29] I. H. Abbott and A. E. Von Doenhoff, Theory of Wing Sections, New York: Dover, 1959.

[30] F. Sherman, Viscous Flow, New York: McGraw-Hill, 1990.

[31] K. Karamcheti, Principles of Ideal-Fluid Aerodynamics, Malabar: Krieger, 1980.

[32] O. G. Tietjens, Applied Hydro- and Aerodynamics, based on the lectures of L. Prandtl, New York: Dover, 1934.

[33] B. Heine, K. Mulleners, G. Joubert and M. Raffel, "Dynamic Stall Control by

Passive Disturbance Generators," in *29th AIAA Applied Aerodynamics Conference*, Honolulu, 2011.

APPENDICES

APPENDIX A - MATLAB CODE

```
%The "for" loop reads each of the images, applies the
filters, shows the
%images for verification, and then writes the new image
data to a file name
%beginning with "output\" followed by the original file
name

files = dir('*.png');
grid = imread('input\points.bmp');

for k = 1:numel(files)
    I = imread(files(k).name);
    CG = imcrop(I,[0 0 1377 751]);

    f = fspecial('motion');
    FG = imfilter(CG,f,'replicate');

    f2 = fspecial('average');
    SG = imfilter(FG,f2,'replicate');

    f3 = fspecial('unsharp');
    SG = imfilter(SG,f3,'replicate');

    overlay = grid + SG;

    %figure; imshow(overlay); title('Overlay Image');

    imwrite(overlay, ['output\' files(k).name]);

end
```

APPENDIX B - ADDITIONAL FIGURES

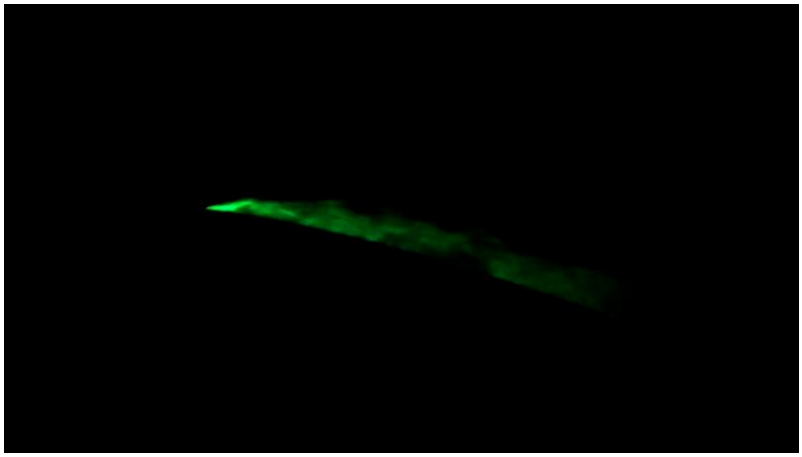

Figure 40. NACA-0012 data at 15^{o}; large VGs at 1.2 spacing.

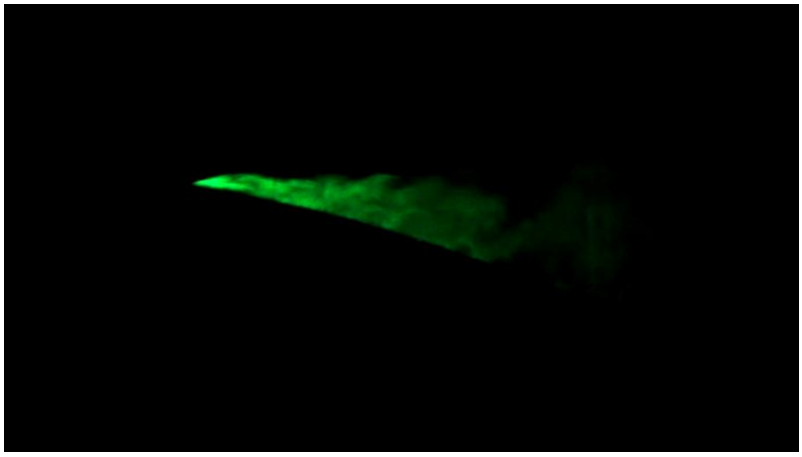

Figure 41. NACA-0012 data at 15^{o}; large VGs at 1.6 spacing.

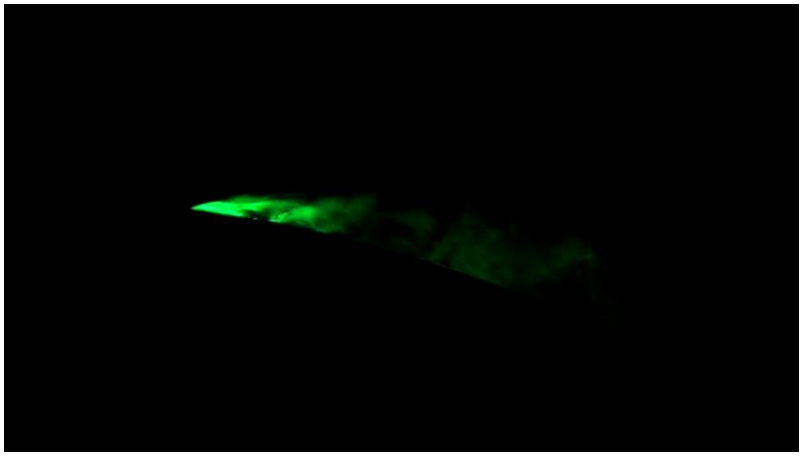

Figure 42. NACA-0012 data at 15^{o}; large VGs at 3.2 spacing.

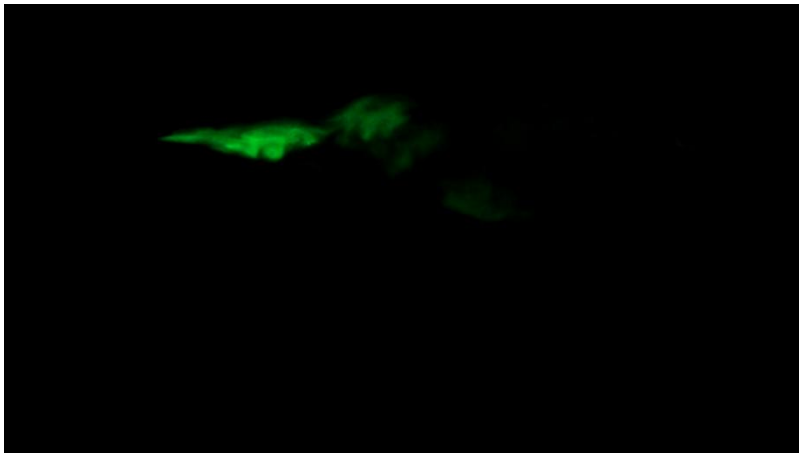

Figure 43. NACA-0012 data at 15^{o}; medium VGs at 1.2 spacing.

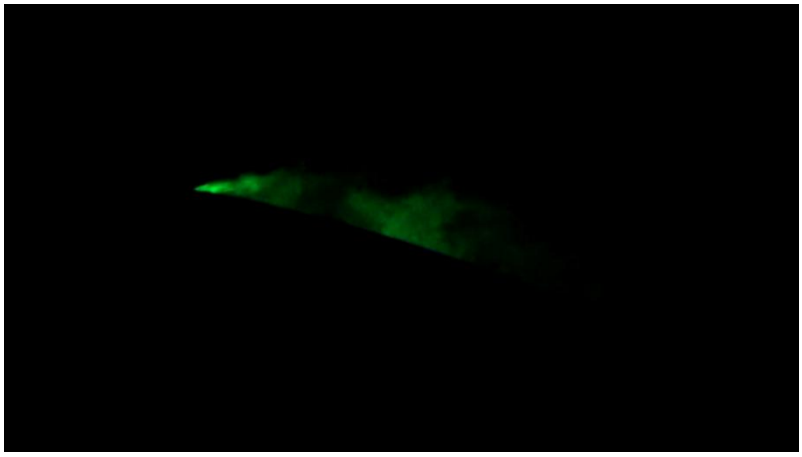

Figure 44. NACA-0012 data at 15^{o}; medium VGs at 1.6 spacing.

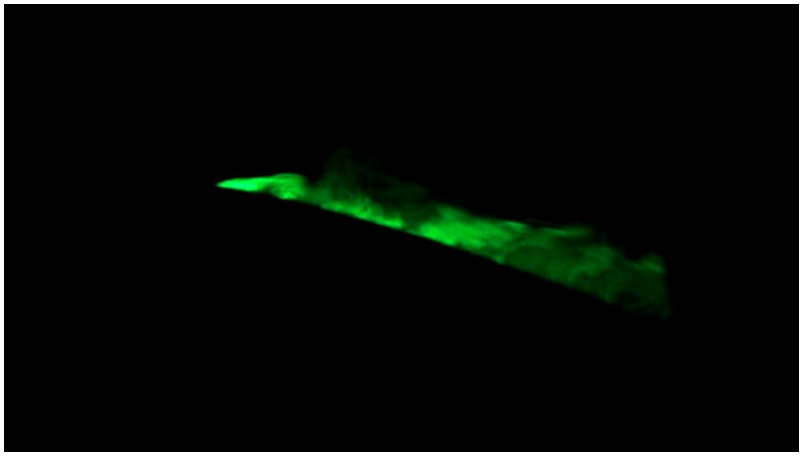

Figure 45. NACA-0012 data at 15^{o}; medium VGs at 3.2 spacing.

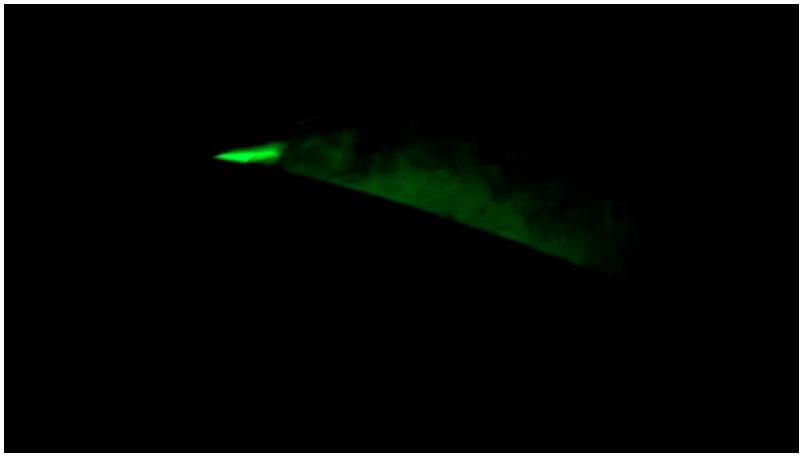

Figure 46. NACA-0012 data at 15^{o}; large VGs at 1.2 spacing.

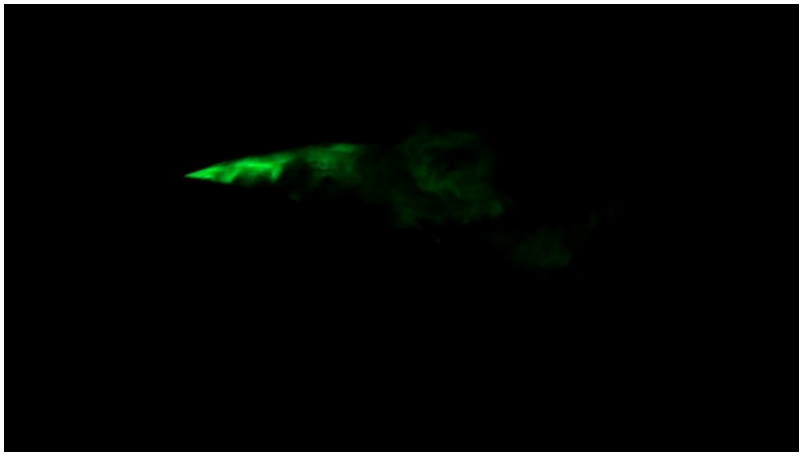

Figure 47. NACA-0012 data at 15^{o}; large VGs at 1.6 spacing.

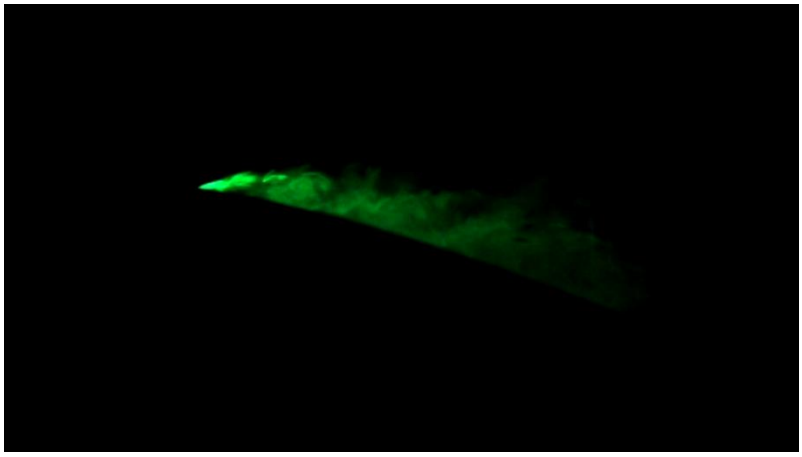

Figure 48. NACA-0012 data at 15^{o}; large VGs at 3.2 spacing.

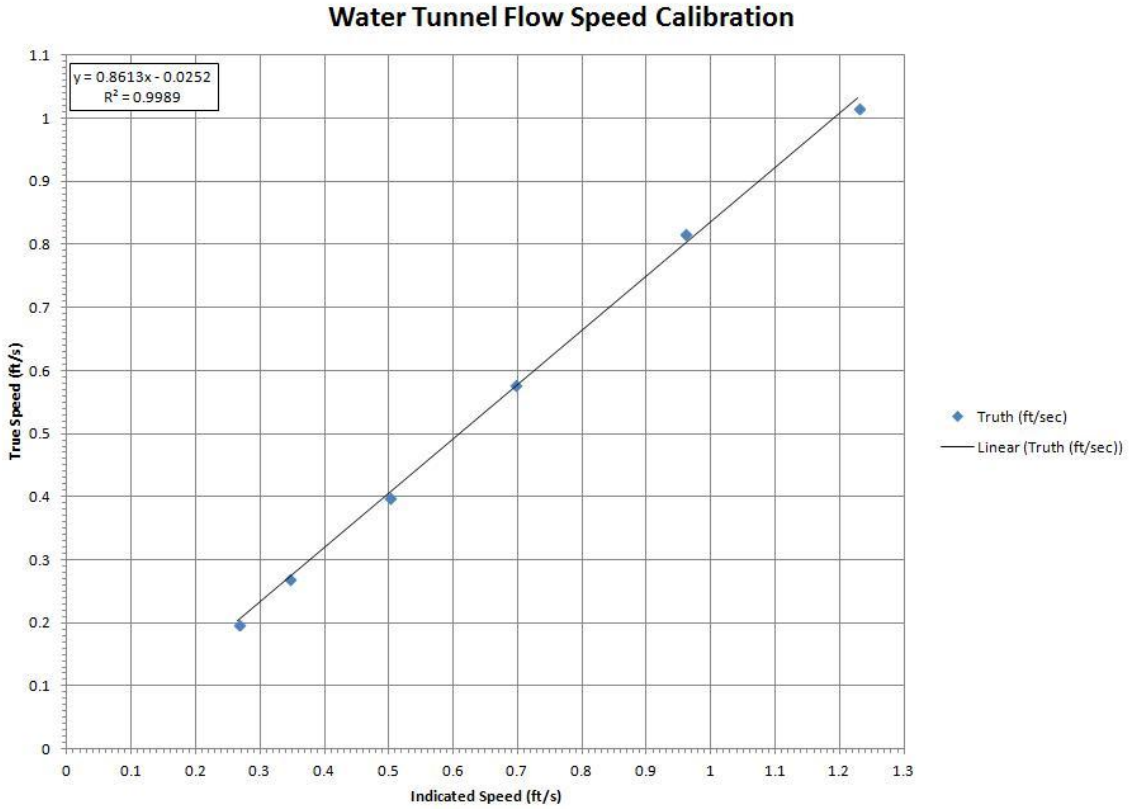

Figure 49. Calibration curve for flow meter.

VITA

David Joseph Ronald Tucker was born in St. John's, Newfoundland, Canada on June 15, 1980. He was raised in Newfoundland; first Grand Bank and then Kippens, and graduated from St. Stephen's High School in Stephenville in 1998. After a year in St. John's, Newfoundland in first year engineering at the Memorial University of Newfoundland (MUN), he enrolled in the Canadian Forces Regular Officer Training Plan (ROTP), completed Basic Officer Training in St-Jean, Quebec and began studies at the Royal Military College of Canada in Kingston, Ontario. He graduated with a Bachelor of Engineering Degree (Mechanical) in May 2003 and was promoted to Second Lieutenant.

Upon completion of the Aerospace Engineering Officer Basic Course in May 2006, he was promoted to Lieutenant and posted to 12 Air Maintenance Squadron in Shearwater, Nova Scotia to the position of Aircraft Maintenance Support Officer. In June 2008 he was promoted to Captain and moved to 423 Maritime Helicopter (MH) Squadron (Sqn) in the position of Maintenance Operations and Support Officer. He simultaneously acted as the Fleet Air Maintenance Officer on the staff of the Commander - Canadian Fleet Atlantic. In July 2010 he took over A Flight at 423 MH Sqn as the Aircraft Servicing Officer. Throughout his time at 12 Wing Shearwater he also held the secondary position of Wing Air Weapons Safety Officer.

He began studies at the University of Tennessee Space Institute in August 2011, completing all requirements for the degree of Master of Science in Aerospace Engineering. After completion of his studies he will be posted to the Aerospace Engineering Test Establishment in Cold Lake, Alberta.

He is married to Sara Lynn Dobbin of Norris Arm, Newfoundland. In his spare time, David enjoys hiking with Sara and their dog Duke.